PERGAMON

Engineering Fracture Mechanics 69 (2002) 1521–1555

Engineering Fracture Mechanics

www.elsevier.com/locate/engfracmech

Statistical fracture modeling: crack path and fracture criteria with application to homogeneous and functionally graded materials

T.L. Becker Jr. [a], R.M. Cannon [b], R.O. Ritchie [b,*]

[a] *Department of Mechanical Engineering, University of California, Berkeley, CA 94720, USA*

[b] *Department of Materials Science and Engineering, University of California, Berkeley, and Materials Sciences Division, Lawrence Berkeley National Laboratory, Berkeley, CA 94720, USA*

Received 19 February 2001; received in revised form 22 January 2002; accepted 23 January 2002

Abstract

Analysis has been performed on fracture initiation near a crack in a brittle material with strength described by Weibull statistics. This nonlocal fracture model allows for a direct correlation between near crack-tip stresses and failure. Predictions are made for both the toughness and average fracture initiation angle of a crack under mixed-mode loading. This is pertinent for composites and is especially interesting for functionally graded materials (FGMs), where the stress and strength fields vary from the homogeneous form away from the crack tip. Both analytic and finite element analyses of FGMs reveal that gradients in Weibull scaling stress $\sigma_0(x, y)$ usually lead to a dramatic decrease of initiation fracture toughness; moreover, gradients normal to the crack result in a crack growing toward the weaker material. When comparing FGMs with gradients in Young's modulus in the direction of the crack path, $E(x)$, and the same stress-intensity factor K, the crack growing into the steeper negative gradient will be tougher, if m, the Weibull modulus, is low; with growth in the stiff direction, the effect is opposite. These effects offset the higher-stress intensity for cracks growing into more compliant material, and the crack-tip shielding when growing into a stiffer material based upon expectations for the applied load. Perpendicular gradients in modulus can cause a far-field mode I loading to produce mixed-mode loading of the crack tip and other asymmetric adjustments in the stress field; the gradient induces non-coplanar cracking that depends strongly on m. The distribution of damage near a crack tip will vary strongly with m. For high m materials, failure is dominated by the very near-tip parameters, and effects of gradients are minimized. With low m, distributed damage leading to toughening can be exaggerated in FGMs. Finally, consideration is given to the role of several higher-order terms in the stress field.

Keywords: Functionally graded materials; Fracture toughness; Crack kinking; Mixed-mode fracture; Weibull statistics

[*] Corresponding author. Tel.: +1-510-486-5798; fax: +1-510-486-4881.
E-mail address: roritchie@lbl.gov (R.O. Ritchie).

PII: S0013-7944(02)00047-4

Nomenclature

x, y, z	Cartesian coordinates, crack lies along $y = 0$ in x-direction
r, θ	polar coordinates
ξ, ς	coordinate variables
σ_{xx}, σ_{xy}, σ_{yy}	stress components referenced to $\{x, y\}$ coordinate system
σ_{yield}	yield strength
σ_1	maximum principal stress
$\sigma_{\theta\theta}$	Hoop stress
a	crack length
B	characteristic thickness in z direction
K_{I}, K_{II}	mode I and mode II stress-intensity factors
K_{Ic}	plane-strain fracture toughness value
G	strain energy release rate
G_{c}	critical strain energy release rate at fracture
ψ	phase angle of crack tip, $\psi = \tan^{-1}(K_{\text{II}}/K_{\text{I}})$
f^{I}, f^{II}	nondimensional mode I and II functions of θ for elastic crack stresses
f_1^{ψ}	nondimensional function of θ and ψ for elastic crack principal stress
Φ	global failure probability
K_{Φ}, G_{Φ}	probable fracture toughness, K or G, to achieve failure probability Φ
$p(\sigma)$	failure probability in limit of small volume
p^*	volume-weighted failure probability in crack-tip field
m	Weibull modulus
σ_0	Weibull scaling stress
σ_{u}	Weibull cutoff stress
g	function to describe dependence of property variation on location
b, c	gradient parameter, value at crack tip
E	Young's modulus
v	Poisson's ratio
$\bar{x}$, $\bar{y}$	coordinates of average location of crack initiation site
ϕ	angle of average crack initiation event, $\tan^{-1}(\bar{y}/\bar{x})$
f	percentage of fracture initiations occurring between $-\pi$ and θ_f
θ_f	angle defining the fth-percentile of fracture probability
$\bar{r}$	average distance of crack initiation
r_x, r_n	distance of maximum, minimum local failure probability
ρ	cutoff radius near crack tip
R	outer radius of integration for analysis of infinite bodies
F	nondimensional mixed-mode toughness function for homogeneous material
θ_{σ}^*, θ_G^*	optimal kink angles for max $\sigma_{\theta\theta}$ or G criterion
J	Jacobian of mapped quadratic finite element
w_i	Gauss–Legendre integration weights
q	Toughness dependence on radial band (p or R) exponent $= (M - 4)/2m$

1. Introduction

The earliest report on the relationship between the volume of a brittle material and its measured strength is credited to Leonardo Da Vinci, who observed that the strength of a wire in tension decreased as its length increased [1]. Since then, extreme-value Weibull statistics [2] have been developed to model the dependence of probabilistic failure on both applied stress and affected volume of a bulk material. This dependence can explain phenomena such as the enhanced measured strengths of brittle materials in bending vs. those in tension. Similarly, the fracture toughness of material that undergoes a stress-controlled fracture with extension initiated away from a pre-existent crack tip can be predicted by applying Weibull statistical analysis to bodies containing cracks or notches.

One area where Weibull statistics can play a descriptive role is in the fracture of composites or layered materials. Important developing applications in aerospace, power generation, microelectronics and bioengineering demand characteristics that are often unobtainable in any single material. Traditional design of such a material seeks to invoke the desirable characteristics of each of the constituent phases in order to meet such requirements. However, the internal stresses caused by the elastic and thermal properties mismatch at an interface of two bulk materials can mitigate the successful implementation of such composites. To address this problem, FGMs have been developed to satisfy the needs for properties that are unavailable in any single material and for graded properties to offset adverse effects of discontinuities.

The introduction of gradual compositional changes removes large-scale interface-induced stress singularities and can even result in stress-free material joints. This gradual change in composition over length scales that are significant compared to the overall dimensions of the body is what distinguishes FGMs from other composites. The gradient shape is a design parameter determining the behavior of an FGM structure. Associated complications involving spatially varying elastic constants have demanded re-examination of the elastic crack problem. Although the fracture mechanics solutions for stress and displacement fields in homogeneous and continuously graded materials agree in the asymptotic near-tip limit [3], the scope of the material gradient effects on fracture behavior are not well comprehended.

These crack-induced stresses are affected by modulus gradients, however. For example, far-field tensile loading on elastic materials with gradients in modulus can cause mixed-mode (tensile and shear) crack loading. This will obviously influence the extension criteria for the simple situation of cracks in materials that grow continuously from the tip, which are known to kink or deflect when loaded in mixed mode. Alternatively in certain classes of FGMs (e.g., composites), crack extension will entail a nonlocal criteria involving reinitiation some distance away from the crack tip. In such an FGM, these reinitiations will depend on the nonlocal stress field that reflects both the stress-intensity factor and the gradient-induced effects, i.e., an FGM will fracture at a stress intensity, K, different from that in a homogeneous material. Weibull statistical analysis provides a tool for describing the relationship between the probability of fracture and the distributions of stresses and strengths near such a crack; the effects on the crack path of the gradient-induced stresses can also be assessed. Effects on toughness and crack trajectory from gradients in strength can similarly be explored though this framework.

To describe the mixed-mode crack extension criteria of materials governed by Weibull statistics near a prior crack, which is the purpose of this work, relationships for the average location of fracture initiation near an elastic crack tip and for the probable toughness are developed. These relationships are first applied to infinite, homogeneous bodies and results are compared with classical deterministic behavior for kinking and extension in response to stresses exactly at the tip. The analysis is then applied to infinite FGMs. Although the analysis depends on failure initiating at locations away from the crack tip, in both these applications, effects of higher-order terms in the stress field are not considered. In order to test the dependence on conventional geometry-specific stresses away from the crack tip or on gradient induced, higher-order terms, two fracture mechanics specimen geometries with various modulus or strength gradients are examined using the finite element method (FEM).

2. FGM fracture mechanics

A common, although not universal, feature of FGMs is that they are multiphase composites where the microstructure can often be described as a particle of one phase embedded in a matrix of another. In such an FGM, the gradient shape has little influence at small length scales, as the mechanics are dominated by the size, shape and interface conditions of the particle. Continuum mechanics analyses of an FGM usually emphasize the large-scale phenomenon and treat the FGM as a smoothly graded material, employing only "effective" properties of the isotropic homogenized composite at any given location. It is through the variation of these effective material properties (e.g., elastic modulus) that the nature of the spatial variations of the constituents is considered to affect the mechanical behavior of an FGM.

For FGMs with compositions including a brittle phase, e.g., ceramic, intermetallic or glass, fracture is an important design limitation. If an FGM is a brittle/brittle composite (e.g., Mo/SiO_2 [4], Al_2O_3/Si_3N_4 [5], SiC/TiC [6], ZrO_2/Al_2O_3 [7]), linear-elastic fracture mechanics can be used to characterize such failure, providing that effects of the gradient in elastic modulus are accounted along with the heterogeneous nature of the fracture resistance for the multiphase microstructure.

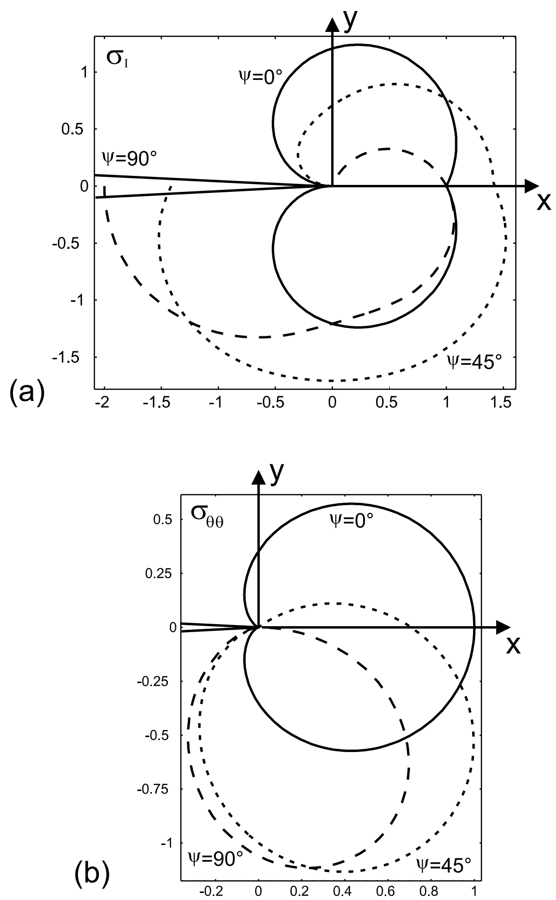

Fig. 1. Isostress contours for (a) maximum principal stress σ_1 and (b) hoop stress $\sigma_{\theta\theta}$ for loading phase angles $\psi = 0°, 45°, 90°$. Contour shapes indicate relative stress levels, with larger r corresponding to higher stress at that θ.

The study of fracture mechanics for FGMs has yielded linear-elastic crack-tip stress field solutions for various elastic gradients and boundary conditions. A fundamental result is that for locations asymptotically close to the crack tip, the stress fields for a homogeneous material and an FGM are identical [8,9]. In this limit, the stresses near the crack tip are described by the singular terms of the classical solution of Williams [10]

$$\sigma \approx \frac{K_{\mathrm{I}} f^{\mathrm{I}}(\theta)}{\sqrt{2\pi r}} + \frac{K_{\mathrm{II}} f^{\mathrm{II}}(\theta)}{\sqrt{2\pi r}} \tag{1}$$

with

$$f^{\mathrm{I}}(\theta) = \left[\cos\left(\frac{\theta}{2}\right)\left(1+\sin\left(\frac{\theta}{2}\right)\right)\right] \quad \text{and} \quad f^{\mathrm{II}}(\theta) = \left[-\sin\left(\frac{\theta}{2}\right)+\sqrt{1-\frac{3}{4}\sin^2\left(\frac{\theta}{2}\right)}\right],$$

for $\sigma = \sigma_1$, the maximum principal stress. Fig. 1 compares isostress contours for principal and hoop stresses for a sharp elastic crack with phase angles of $\psi = 0°$, 45° and 90° ($K_{\mathrm{II}} = 0$, $K_{\mathrm{I}} = K_{\mathrm{II}}$, $K_{\mathrm{I}} = 0$).

As in homogeneous materials, K_{I} and K_{II}, the modes I and II stress-intensity factors, characterize the symmetric and antisymmetric stress fields in the neighborhood of a crack tip; however, their values for a given geometry and load will differ vs. the homogeneous case in both magnitude, $|K| = \sqrt{K_{\mathrm{I}}^2 + K_{\mathrm{II}}^2}$, and phase angle, $\psi = \tan^{-1}(K_{\mathrm{II}}/K_{\mathrm{I}})$ [11].

With variable modulus $E(x, y)$, strains associated with the Williams crack-tip field do not satisfy the equations of compatibility. At finite distances away from the crack tip (where the elastic modulus differs from that at the tip), the solution field must take on a different character. Jin and Batra [12] estimated the size of the near-tip zone over which the stresses of the Williams singularity for homogeneous material will asymptotically govern (the K-dominant region); this is where $(|\nabla E|/E) \ll (1/r)$, $(|\nabla^2 E|/E) \ll (1/r^2)$. Therefore, the steeper the gradient in E, the smaller the region wherein Eq. (1) pertains. Outside the K-dominant regions, the stresses depend on the variation in E, among other factors. However, extant solutions have not been expressed directly in a series form for which the behavior of the next order terms can be readily appreciated.

The mixed-mode analysis of Erdogan and co-workers [3,11] justified describing the asymptotic stress field near a crack by pointwise multiplication of the conventional singular terms by the variation in Young's modulus, in the form $E(x, y)/E(0, 0) = \mathrm{e}^{(\beta x+\gamma y)}$. It is proposed that more generally: [1]

$$\sigma_{ij} \approx \frac{E(x,y)}{E(0,0)}\left[\frac{K_{\mathrm{I}}}{\sqrt{2\pi r}} f_{ij}^{\mathrm{I}}(\theta) + \frac{K_{\mathrm{II}}}{\sqrt{2\pi r}} f_{ij}^{\mathrm{II}}(\theta)\right], \tag{2}$$

for any $E(x, y)$ which is a continuous function of position (taking Poisson's ratio, ν, as a constant). $E(0, 0)$ is the value at the crack tip.

Eq. (2) approximates the effect of modulus variation, $E(x, y)$, on the stress over a wider region than that in which Eq. (1) pertains. Eq. (2) satisfies the equations of compatibility exactly, although it does not satisfy the conditions for equilibrium. It will therefore also be limited in its own region of dominance.

The issue of the direction of crack growth in homogeneous materials was first addressed by Erdogan and Sih [14], who predicted that a crack loaded in mixed mode would kink along an angle, θ_{σ}^{*}, which

[1] See Becker et al. [13] for a derivation of this type of approximations for FGMs with spatially varying Young's modulus.

corresponds to the maximum hoop stress, $\sigma_{\theta\theta}$, at the tip. Later analyses that explored the mode-mixity and strain energy release rate, G, of a kinked crack gave more rigorous results, e.g., the optimal θ_G^* gives maximum G; these converge with the hoop-stress criteria at small kink angles (see discussions by Cotterell and Rice [15] and Hutchinson and Suo [16]). The first analysis of crack kinking in FGMs [17] was limited to application of the first-order homogeneous analysis of Cotterell and Rice [15]; implicit here is the assumption that the gradient in Young's modulus only affects the crack tip through mode-mixity, ψ. This is true for crack kinks of infinitesimal length growing continuously from the tip, but these assumptions cannot be sustained if material inhomogeneity leads to longer kinks or for fracture events that are initiated ahead of the crack tip in materials with variable strength. Recently, an FEM analysis by Becker et al. [18] revealed information about adjustments in the stress field that arise from a sigmoidal gradient in elastic modulus aligned normal to a small crack. In this instance, ψ changes over a dimension $r \sim 1/b$, attaining its asymptotic value for $rb < 0.2$, where $b \approx |\nabla E|/E$ is the gradient coefficient. In contrast, a T-like stress term that adjusts σ_{xx}, only emerges at much smaller dimensions, i.e., at $r < 1/10b$, and does not approach its asymptotic limit until far smaller values of r; it influenced kink angles, θ_G^*, even for $rb \sim 0.01$. This gradient-induced T-stress depends strongly on externally applied shear loading [18], unlike the T-stress for homogeneous materials that describes an increment in σ_{xx} that is independent of position [10,19].

3. Ritchie–Knott–Rice fracture modeling

3.1. Weibull statistics

The effects of variability in strength of brittle materials can be described using extreme value statistics [2]. For a body experiencing spatially variable stress σ, the probability of failure Φ, is

$$\Phi = 1 - \exp\left[\int_{\mathrm{Vol}} -\frac{p(\sigma)}{V_0}\,\mathrm{d}V\right], \tag{3}$$

where V_0 is a reference volume and $p(\sigma)$ the strength distribution, i.e., the cumulative failure probability in the small-volume limit. The three-parameter Weibull strength distribution has the form:

$$p(\sigma) = \begin{cases} \left(\dfrac{\sigma_1 - \sigma_u}{\sigma_0}\right)^m & \text{for } \sigma - \sigma_{\mathrm{u}} > 0, \\ 0 & \text{for } \sigma - \sigma_{\mathrm{u}} \leqslant 0, \end{cases} \tag{4}$$

where σ_1 is maximum principal stress and σ_{u}, σ_0 and m are material constants to be determined by experiment. The lower bound cutoff strength, σ_{u}, is often set to zero for ceramics and glasses, thus defining the two-parameter Weibull distribution, where σ_0 is the scaling strength.

The Weibull function expresses the failure probability in terms of both the stress level and the volume over which stress is distributed. The severity of this volume dependence is largely determined by the Weibull modulus, m. [2] In the limit of a purely deterministic material, as $m \to \infty$, failure is dictated by the maximum stress at any point, with no scatter. For a high-quality engineering ceramic, m is in the range of 20–50. However, for brittle/brittle composites, the presence of internal interfaces, local residual stresses, and more microstructural variability often produce greater scatter in strength and so lower Weibull modulus. Indeed, bend tests of a SiO_2/Mo FGM have indicated a Weibull modulus of 4 pertains [20].

[2] The cutoff stress σ_{u} also can mitigate the effect of volume. When a two-parameter distribution is applied to an infinite body, any nonzero far-field stress leads to a failure probability of unity. Invoking a cutoff stress allows modeling of failure in an infinite body.

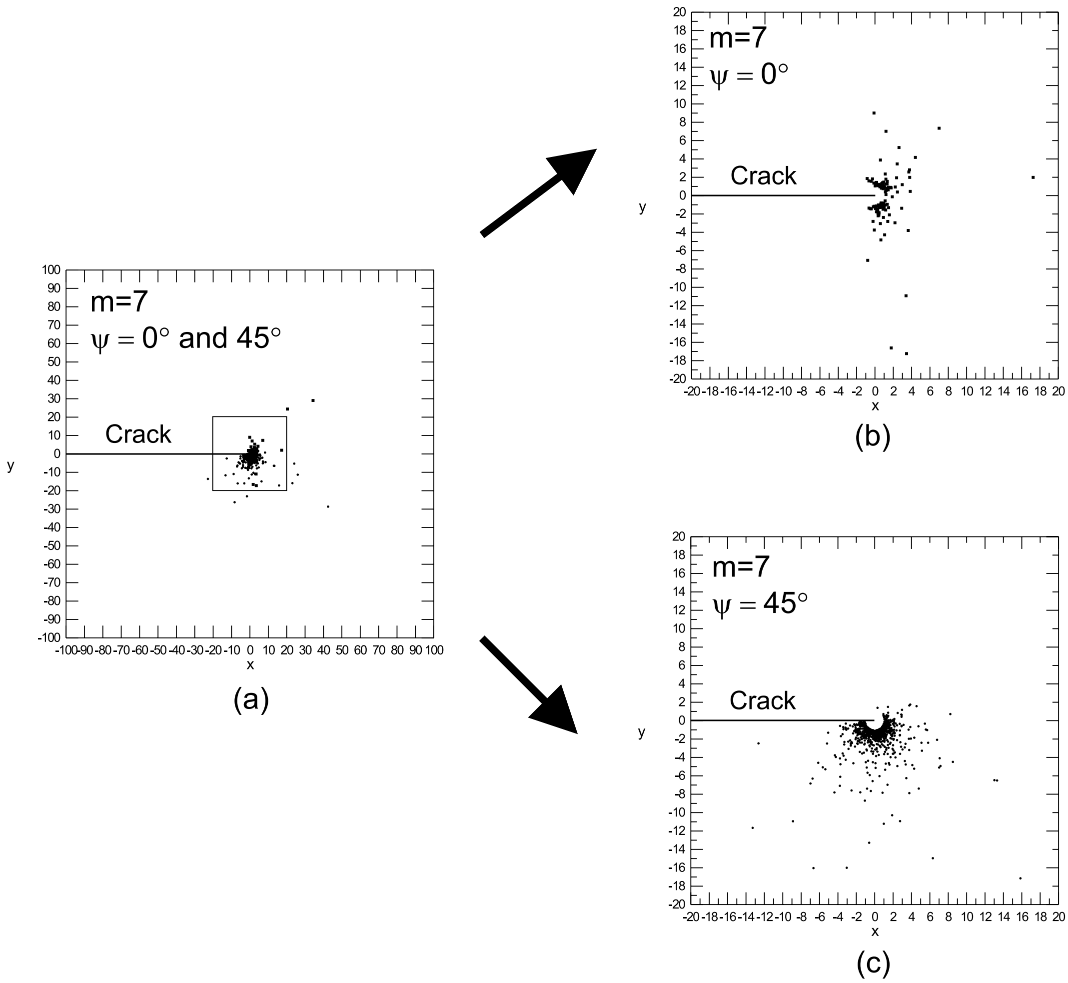

Fig. 2. Results of Monte Carlo simulations for a brittle material near a sharp elastic crack. Mode I, ($\psi = 0°$, square symbols) and mixed-mode ($\psi = 45°$, circles) cases are displayed for Weibull modulus, $m = 7$. Points around the crack tip indicate the location of a simulated fracture initiation. Strong skewing toward the negative y-direction is evident for the mixed-mode case, as is the greater number of fracture initiations indicating a decreased toughness.

To demonstrate characteristic fracture initiation behavior near a crack in a homogeneous material with strength described by Weibull statistics using the maximum principal stress, Fig. 2 displays the results of Monte Carlo simulations (details are in Appendix A). Each point indicates the location of a fracture initiation for mode I (square symbols) and mixed mode, $\psi = 45°$, (circles) loading. First, for the mode I case, these data are scattered away from the x-axis, but are roughly symmetric about $y = 0$, giving a bimodal distribution with an average angle of 4°. For the mixed-mode case, the data are strongly skewed toward the negative y-direction, at an average angle of $-81°$, and failures are found near the crack flank where $\sigma_{\theta\theta}$ vanishes. This indicates that, based on averaging several events, there are tendencies for straight-ahead crack extension under mode I loading and downward growth under positive phase-angle loading. In addition, for the same number of trials, the number of fracture initiations under mixed-mode loading exceeds that for mode I loading at the same $|K|$ (764 sites vs. 111). This indicates a lower resistance to fracture initiation pertains at a given magnitude of stress intensity. This would result in a lower measured fracture toughness. A framework for quantifying such expected trends is needed.

3.2. Statistical fracture modeling

Nonlocal, statistical crack extension criteria have been successfully applied for marginally brittle metals but can be problematic, even if appealing, for purely elastic materials. The near-tip region of a crack is an extreme example of the competition between stress and volume. At the tip of a sharp elastic crack, stress is infinite but is experienced over exactly zero volume. Away from the crack tip, an increasing volume is exposed to decreasing stress. The Ritchie–Knott–Rice (RKR) fracture model [21] in part used this competition to motivate the description of fracture toughness and its variability in low-toughness steels in terms of the stresses at a "characteristic distance" ahead from the crack tip, where fracture of a brittle inclusion or particle triggers catastrophic crack growth.

The direct substitution of singular fracture mechanics stress fields into Eq. (3) yields an integral that is not finite for most values of Weibull modulus. [3] This means that for any applied load, the global failure probability would be unity and the fracture toughness would be zero. A number of arguments or adjustments have been invoked to avoid this nonphysical result.

For materials with sufficient ductility, crack-tip blunting truncates the stresses near the tip and renders the integral (Eq. (3)) finite. Numerical calculation [23] of a blunted stress field has been performed as well as pseudo-analytic application [24] of a plastic notch field within the HRR singularity [25,26].

For elastic sharp cracks, special attention must be paid to the physical implications of applying Eq. (3) near the crack tip. Regardless of the mechanism underlying the statistical fracture process, the characterizing statistical parameters of the strength distribution will depend upon the volume of material tested to obtain them. When this volume is smaller than can be expected to possess any of the dominant fracture elements (carbide particle in low-toughness steels, grain boundary, etc.), the subsequent failure will no longer be described by the same parameters as is the bulk material even if it is statistical in nature. Such small volumes are likely to be stronger than implied, and may contribute little incremental probability of failure. The implications of applying the Weibull distribution to the region of small volume and high-stress gradient near the crack tip led Beremin [27] to invoke a cutoff radius around the crack tip, which was excluded from the region of integration. Evans [28] ruled out the classical Weibull equation for $p(\sigma)$ on related physical grounds and analyzed a sharp crack tip with a substitute $p(\sigma)$. Alternatively, the explicit modeling of a notch rather than a sharp crack allows for integration of the stress field over the entire material region, using Eqs. (3) and (4) with the results depending the notch size [23,29].

Previous authors (e.g., Refs. [22,24,28]) have investigated the incremental failure probability ahead of a crack tip, with the distance having the maximum failure probability deemed to be a characterizing parameter. These analyses utilized the first term of a stress field expansion (either Williams or HRR) within an infinite body, which also required the use of a far-field cutoff criteria.

3.3. Crack trajectory

For mixed-mode fracture, considering the single distance of maximum failure probability is insufficient compared to analyzing the full planar stress field. Although analyses of continuous crack kinking use the hoop stress $\sigma_{\theta\theta}$ as the determinant of kink angle, θ^*_σ, and critical load, for initiation of further cracking at a distance away from the main crack tip, the flaws need not be aligned along lines of constant θ. Thus,

[3] For the linear-elastic solution, the integral is not defined for ($m > 4$). In nonlinear materials, a similar result depends on m and the strain-hardening coefficient [22].

the principal stress σ_1 is used to determine flaw activation. The mode I elastic stress field possesses maxima in σ_1 at $\theta = \pm 60°$; symmetry dictates that mode I crack advance must occur along $\theta = 0°$, but only statistically.

The expected location of the activated flaws is described from a spatial average of the failure probability. With spatially varying stress, the average of such a coordinate ξ is

$$\bar{\xi} \equiv \frac{\int_{\mathrm{Vol}} \xi \frac{p(\sigma)}{V_0}\,\mathrm{d}V}{\int_{\mathrm{Vol}} \frac{p(\sigma)}{V_0}\,\mathrm{d}V}. \tag{5}$$

When $\xi = x$, $\xi = y$, the mean Cartesian coordinates, $\bar{x}$ and $\bar{y}$, of the fracture initiation are obtained. From these, the angle from the $y = 0$ plane of the average location can be described as $\phi \equiv \tan^{-1}(\bar{y}/\bar{x})$. Eq. (5) also yields the mean distance $\bar{r}$ for $\xi = r$. (This is, in general, distinct from, and usually exceeds, the radial coordinate of the average location, $\sqrt{\bar{x}^2 + \bar{y}^2}$.)

It is possible to describe the relative contribution of stress fields laying at different angles to the total failure probability. The median angle that bisects the angular distribution of failure probability, θ_{50}, is defined through

$$\frac{\int_{-\pi}^{\theta_f} p(\sigma)\,\mathrm{d}\theta}{\int_{-\pi}^{\pi} p(\sigma)\,\mathrm{d}\theta} = f\Phi, \tag{6}$$

with $f = 50\%$. Furthermore, bands of probability can similarly be defined, so that the proportion of the failure probability between two angles is determined, i.e., 90% of failures will be initiated between θ_5 and θ_{95}.

4. Procedures

Calculations for infinite bodies were performed with stresses derived from Eq. (2). Eqs. (5) and (6) were evaluated with the numerical integration package in Mathematica 3.0 (Wolfram Research, Champaign, IL, USA). To evaluate finite geometries, the single edge-crack tension (SE(T)) and middle-crack tension (M(T)) fracture mechanics specimens were modeled by the FEM. A plane-strain linear-elastic finite element code FEAP 4.2 [30] was modified such that during integration of the stiffness matrix, the elastic constants were evaluated at each of the Gauss points (3 per direction, 9 total). This allowed for quadratic variation in modulus to be modeled within a single element.

The crack length, a, was kept constant in the FEM analyses, being equal to half the total width of the sample in the x-direction, W. The mesh for the M(T) sample was the same as for the SE(T) sample (Fig. 3), except it contained an additional row of displacement boundary conditions along $x = -a$, preventing displacements in the x-direction. The mesh consisted of 2300 total elements, 9233 nodes, with extensive refinement using a fan array in the near-tip region, with the smallest element size on the order of $a/10^6$. The fracture mechanics element of Stern and Becker [31] was used in both meshes to model the first ring of elements surrounding the crack tip. A second mesh with 4096 elements was also used to estimate the error via refinement. The difference between the results from the two meshes was negligible, with average initiation angles differing by <0.1°.

Stress-intensity factor calibrations were performed for each geometry and gradient. Pointwise evaluation of the stress-intensity factors can be obtain through

$$\left\{ \begin{matrix} K_{\mathrm{I}} \\ K_{\mathrm{II}} \end{matrix} \right\} = \sqrt{2\pi r} \begin{pmatrix} f_{xy}^{\mathrm{I}}(\theta) & f_{xy}^{\mathrm{II}}(\theta) \\ f_{yy}^{\mathrm{I}}(\theta) & f_{yy}^{\mathrm{II}}(\theta) \end{pmatrix}^{-1} \left\{ \begin{matrix} \sigma_{xy}(r,\theta) \\ \sigma_{yy}(r,\theta) \end{matrix} \right\}. \tag{7}$$

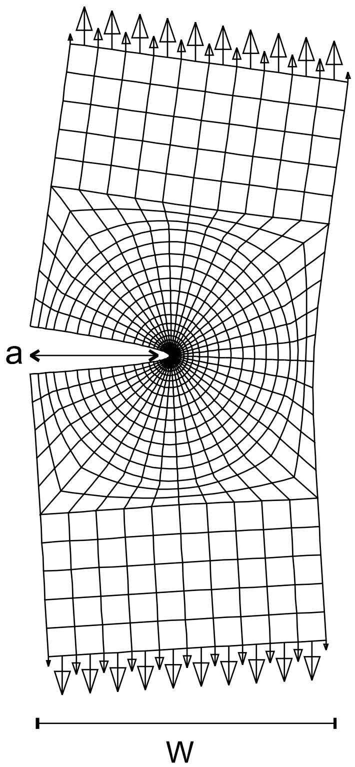

Fig. 3. Finite element mesh used in study of SE(T) fracture mechanics specimen. A high degree of refinement was used, with a focused ring of elements surrounding the crack tip. A similar mesh with different boundary conditions was used for the M(T) sample.

Excluding the crack flanks and the first four elements at the crack tip, these values were averaged over Gauss points within the next five rings of elements (360 elements total, those for $-160° < \theta < 160°$ and $1/10^5 < r/a < 1/10^4$). The precision of these results found to vary weakly with variance of this fitting region. The results of Becker et al. [18] elaborate the need to fit in a range of $rb < 0.01$ in order to avoid effects of higher-order terms (and see Fig. 14).

The statistical modeling used results from each FEM calculation in the probability integral as the sum over the finite elements, where for a variable ξ,

$$\int_{\mathrm{Vol}} \xi \left(\frac{\sigma}{\sigma_0} \right)^m \frac{\mathrm{d}V}{V_0} \approx \frac{B}{\sigma_0^m V_0} \sum_j^{\mathrm{elems}} \xi_i \left[\sum_i^{\mathrm{Gauss\,pts}} (\sigma_1^m)_i J w_i \right]_j, \tag{8}$$

where J is the Jacobian of the mapped element (calculated at the Gauss points), w_i's are the weights for Gauss–Legendre quadrature, and B is an out-of-plane thickness. For a physical sample with a large thickness, multiple fracture events are sometimes expected to occur along the crack front, with implications discussed in Section 5.1.

Sigmoidal variation in modulus or strength was employed via a function $g(x)$ or $g(y)$:

$$g\begin{pmatrix} x \\ y \end{pmatrix} = (c-1)\tanh\left(b \begin{pmatrix} x \\ y \end{pmatrix} \right) + c. \tag{9}$$

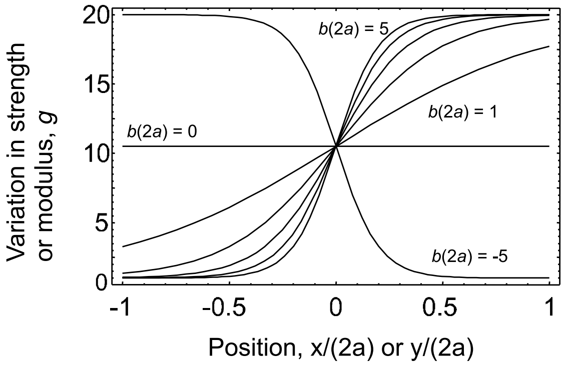

Fig. 4. Sigmoidal gradients modeled. This shape allows for an arbitrarily steep gradient at the crack tip, determined by the parameter b. The total range of variation within the sample is held constant, with $g(\infty)/g(-\infty) = 20$.

At the origin (usually, the crack tip), $g(0) = c$. A value of $c = 10.5$ was chosen for the present analyses, providing a 20-fold change in properties across the sample. As such, b, which was varied, is a measure of the gradient steepness and $(\nabla g/g(0)) = (b(c-1)/c) \approx b$. In the limit of $b \to \infty$, a sharp interface is formed, with $g(\infty)/g(-\infty) = 2c - 1$. Fig. 4 displays shapes of the gradient for a range of b. The Weibull modulus was investigated as a variable but kept constant in any sample.

5. Results and discussion

5.1. Homogeneous infinite body analyses

Application of the Weibull crack initiation model to material with a mode I crack permits description of the fracture toughness using statistical parameters (σ_u, σ_0 and m) and perhaps other material parameters. Extending the analysis to mixed-mode situations allows predictions about homogeneous material response without specific reference to geometry effects.

5.1.1. Mixed-mode fracture toughness

Combining Eqs. (1), (3) and (4) and inverting gives an expression for the stress intensity to produce a given failure probability, K_Φ:

$$K_\Phi = \frac{\sigma_0 (V_0/B)^{1/m} \sqrt{2\pi} (-\ln(1-\Phi))^{1/m}}{\left[\int_{-\pi}^{\pi} f_1(\theta,\psi)^m \, \mathrm{d}\theta\right]^{1/m} F(m,R,\rho)}, \tag{10a}$$

$$F = \begin{cases} \left[\dfrac{R^{2-(m/2)} - \rho^{2-(m/2)}}{2-\frac{m}{2}}\right]^{1/m} & \text{for } m \neq 4, \\ \left(\ln\left(\dfrac{R}{\rho}\right)\right)^{1/4} & \text{for } m = 4, \end{cases} \tag{10b}$$

where $f_1(\theta,\psi) = \sigma_1\sqrt{2\pi r}/|K|$ and can be inferred from Eq. (1). The integration is conducted over an annulus between the inner cutoff radius, ρ, and the outer radius, $R \gg \rho$, which is still within the K-field (Eq. (1)). Explicit values of K_Φ scale primarily with $\sigma_0(V_0/B)^{1/m}\rho^{(m-4)/2m}$ for large m and $\sigma_0(V_0/B)^{1/m}/R^{(4-m)/2m}$ for small m. That is, for materials with large scatter in strength, toughness is dictated by the large volume of

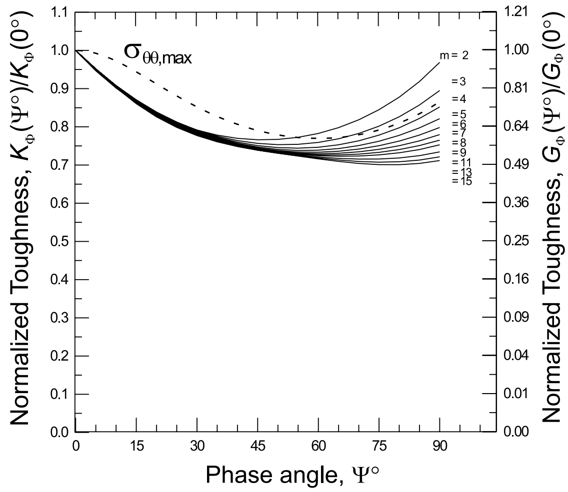

Fig. 5. Prediction for the mixed-mode toughness for an infinite body of a homogeneous material based on statistical fracture model for various values of Weibull modulus (solid lines) compared to the deterministic prediction based on critical hoop stress (dashed line).

low-stress material as $r \to R$; with little scatter, toughness is determined by the small volume of highly stressed material nearest to the crack tip.

From these results, geometry-independent predictions of the relative fracture toughness for mixed-mode loading are shown in Fig. 5 in terms of $|K_\Phi|$ or G. These toughnesses (being normalized to the mode I toughness and thereby independent of the choice of Φ, for fixed R and ρ) predict (for a nonlocal, stress-controlled failure mechanism) a reduction in fracture toughness under mixed-mode loading. Comparing the isostress contours for $\psi = 0°$ and 45° in Fig. 1 explicates this behavior. The area contained within the 45° contour is plainly larger than that of the 0° contour. This can be interpreted as a larger volume being exposed to a given stress level at a given G, or an elevation of stress at a fixed distance, r, from the crack tip. For a material described by initiation at a distance, this lessens the fracture toughness. This reduction in toughness under mixed-mode conditions at moderate phase angles is stronger than that for a deterministic analysis based on the maximum $\sigma_{\theta\theta}$ [14]. Note these $|K_\Phi|$ and G values describe self similar extension of an unkinked crack; the values plotted for critical $\sigma_{\theta\theta}$ approximate the loading that gives an invariant K_{Ic} or G_c at the tip of an optimal kink for continuous crack extension.

5.1.2. Mixed-mode initiation angle and distance

Under mixed-mode conditions, a crack will not, in general, grow in a self-similar manner; rather it will kink off of the $y = 0$ plane. The average initiation angle ϕ calculated via Eq. (5) as $\tan^{-1}(\bar{y}/\bar{x})$ for a crack sustaining mixed-mode stresses in an infinite homogeneous body is shown in Fig. 6. The predicted average crack angles from the statistical formulation based on principal stresses are more negative for $\psi > 0$ and any m than those derived for the continuous growth of the crack tip along the path of maximum $\sigma_{\theta\theta}$, i.e., θ^*_σ [14], or maximum G, i.e., θ^*_G [32], also shown. At higher m, these average initiation angles $-\phi$ increase toward the trend, also plotted, for the angle of maximum principal stress. However, the behavior would only replicate this for extremely large m. Median angles, θ_{50}, exhibit similar trends as does ϕ.

This behavior is easily related to the mixed-mode stress fields plotted in Fig. 1. With pure mode II loading ($\psi = 90°$), the largest principal stress lays along $\theta = 180°$ and locations of average fracture tend toward this extreme. The boundary conditions dictate that this is the σ_{xx} component. Deterministic, continuous-growth analyses predict opening along radial lines and are restricted to the $\sigma_{\theta\theta}$ component, which is zero at the crack flank. This difference requires careful physical interpretation, as discussed in Section 5.1.3.

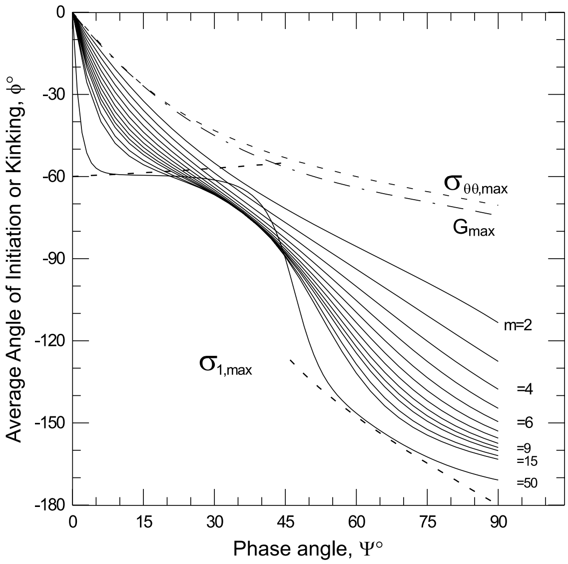

Fig. 6. Average initiation angle for mixed-mode fracture loading for an infinite homogeneous material based on statistical model. Also included are angles of maximum hoop stress and maximum energy release rate criteria (dashed lines).

Table 1
Approximate average distances for fracture initiation

m	2	3	4	7	8	10	16
$\bar{r}$	$R/2$	$R/3$	$R/10$	3ρ	2ρ	1.5ρ	1.2ρ

The mean distances of fracture initiation $\bar{r}$ in an infinite body, also calculated via Eq. (5), are listed in Table 1; these are combined results for $R/\rho = 10^3$ and 10^5. With small values of m (2–4), $\bar{r}$ scales with the outer limit of integration R, $\bar{r} \sim R/2$ to $R/10$. For larger values, $m > 7$, $\bar{r}$ is on the order of the inner cutoff limit of integration ρ, $\bar{r} \sim \rho$ to 3ρ, as is also depicted in Fig. 2. Results are independent of mode mixity.

For small m, the volume is a determinant, and for $m = 2$, the failure probability in a thin annulus at a given r is uniform from the crack tip to infinity in the K-field. Hence, the mean distance is the average of the integration limits $(R + \rho)/2 \approx R/2$. Taking the limit of large m, fracture is dictated simply by the largest stress, that at $\{r, \theta\} = \{\rho, \pm 60°\}$ for $\psi = 0$, but even for $m > 11$, $\bar{r}$ measurably exceeds ρ ($\sim 1.5\rho$). Thus, the first principal stress σ_1, not the hoop stress, is still the pertinent determinant for failure, as $\sigma_1 \geqslant \sigma_{\theta\theta}$ and flaws are expected to be oriented randomly, not along θ.

5.1.3. Relevance and physical implications

The present model is formally limited to calculating the behavior of the first activated flaw, but this ‘‘first failure’’ may or may not cause catastrophic crack growth. For flaw-intolerant materials such as glasses and fine-grained ceramics, initial flaw growth and catastrophic failure generally are synonymous. However, there is experience with brittle, polycrystalline or composite materials with low-Weibull modulus that near-tip microcracked regions can develop [33,34] or especially that cracks bifurcate extensively [35]. Evidently, flaws exist that are activated by the near-tip stress field, but do not yet possess the driving force necessary to overcome the next higher-length scale fracture resistance (e.g., after cracking a weak or residually stressed grain boundary). The statistical initiation analysis (Fig. 6) shows that such a flaw is unlikely to be located on the trajectory followed by a crack under the same loading conditions but that is continuously moving according to the maximum-$\sigma_{\theta\theta}$ (or G) condition (i.e., $\phi \neq \theta^*_\sigma$ for $\psi > 0$). Even in the mode I case where the statistical and continuous-growth analyses agree on the average angle, most of the microcracks will be initiated at large angles to the crack plane.

When failure ensues from growth of a flaw ahead of the main crack, then further extension will eventually involve connection of this flaw and the main crack. The intervening ligament between the main crack and the microcrack will invariably be fractured or torn under mixed-mode loading requiring much greater dissipation [36]. Moreover, if various flaws along the crack front are triggered prior to criticality, which is more likely with larger B and smaller m, they will each surely be at different angles to the crack plane. Thus, the main crack and the microcracks may not immediately link, but rather a microcrack may next grow forward whilst the uncracked ligaments act as bridges and further enhance the toughness [37]. By such interactions and stress shielding, microcracking can be a toughening mechanism in ceramics [38,39] or more likely serves as a trigger to more potent bridging mechanisms [40,41].

Further analysis of the width of the distribution of initiations can be descriptive of the spatial arrays of microcracks that can develop and their potential for toughening. For mode I loading, only 50% of the fracture initiations ($\theta_{75} - \theta_{25}$, Eq. (6)) occur in a band that spans 120° symmetrically about 0°. Although there is little effect of Weibull modulus, it has a much greater effect for mixed-mode loading, with the 50% band spanning 73° for $m = 3$ and only 21° for $m = 11$ as $\psi \to 90°$. A wide dispersion in angles may be indicatory of tough material involving rising R-curves, as is $\phi \neq \theta^*_\sigma$, θ^*_G. However, the problem of treating subsequent failure after first fracture requires an entirely different statistical formulation and detailed simulation of a noncontinuum microstructure with crack–crack interactions [42], which exceeds the present scope.

Thus, very low-m materials, being highly variable locally, can be relatively notch-insensitive globally, with large volumes of low-stress material dominating the probability analysis. For finite geometries, failure would be influenced by stresses outside the K-field, so trends illustrated here are semi-quantitative, even for first fracture, and their application would be geometry dependent. This effect could be somewhat mitigated by the invocation of a cutoff stress σ_u in the Weibull strength distribution (Eq. (4)). Indeed the size of flaws implied by the absence of a cutoff stress becomes unrealistic. This would offset some of the pathological behavior when analyzing cracks in infinite bodies ($K_\Phi \propto R^{-q}$, Eqs. (10a) and (10b)) and may lead to instances where the important behavior occurs within the K-field and more closely reflects trends predicted here, i.e., the pertinent outer cutoff radius should vary as $R \propto 1/\sigma_u^m$.

For large m, one would expect the material to behave in a deterministic manner. Nonetheless, the transition of the fracture mechanism from dictation by σ_1 to $\sigma_{\theta\theta}$ does not follow simply by taking the limit of large m for the present formalism. Thus, this statistical fracture model is unlikely to apply for single phase materials without distributions of internal heterogeneities. Moreover, the nonlocal behavior for intermediate m may be implausible regarding the strength characteristics implied for small volumes under high stress, e.g., near a crack. For example, elementary calculations show that for structural ceramics, the strength implied for small volumes using typical Weibull parameters underestimates the theoretical strength.

For this model to pertain for an intermediate m (>5) material implies that failure does initiate near or beyond some nonatomistic cutoff radius and that $K_\Phi \propto \rho^q$ behavior does occur. Clearly, for semi-brittle materials wherein crack-tip blunting leads to diminished stresses in a region within $r \sim 2K^2/(\sigma_{\text{yield}}E)$ [43], the present type of approximation (perhaps using an HRR stress field) may be robust. For more brittle composites, the lower theoretical strength of impure interfaces [44] and higher internal mismatch stresses compared to a monolithic ceramic could lead to a small interface flaw (off the main tip, but still influenced by the stress concentration of it) reaching criticality before the main crack. Then, it may be possible to conceive ρ as being related to the volume wherein Eqs. (3) and (4) fail, and, moreover, that the quantity $\sigma_0(V_0/B)^{1/m}\rho^{(m-4)/2m}$ can serve as a useful scaling parameter for K_Φ.

5.2. FGM infinite body analyses

In the prior section, analysis was limited to the classical K-field within homogeneous materials. For cracks in graded materials, the stress and/or strength field at a distance away from the crack will vary with the severity of the gradient, and the location and orientation of the crack relative to the gradient. The fracture of an infinite FGM can be modeled similarly, addressing failure probabilities within the context of adjusting a region lying within a K-field by introduction of Eq. (2) into the statistical analysis of Eqs. (3)–(6) and using Eq. (9) to describe gradients in $E(x,y)$ and σ_0. Then, the two-parameter probability function is

$$p(\sigma(r)) = \left\{ \frac{\left[\dfrac{(c_E-1)\tanh\left(b_E(\xi-\xi_o)\right)+c_E}{(c_E-1)\tanh(b_E(\xi_o))+c_E}\right]|K|f_1(\theta,\psi)}{\left[\dfrac{(c_\sigma-1)\tanh(b_\sigma(\varsigma-\varsigma_o))+c_\sigma}{(c_\sigma-1)\tanh(b_\sigma(\varsigma_o))+c_\sigma}\right]\sigma_0(0)\sqrt{2\pi r}} \right\}^m. \tag{11}$$

This is written to simultaneously allow sigmoidal gradients in both σ_0 and E (characterized by b_σ and c_σ and b_E and c_E, respectively, but with m invariant for simplification); these are aligned along angles θ_σ or θ_E, respectively, and can be offset from the crack tip by ς_o and ξ_o. Situations of gradients in either σ_0 or E aligned parallel or normal to the crack plane with the crack tip centered in the gradient (ς_o, $\xi_o = 0$) are examined first. For these, toughnesses are normalized to that from Eqs. (10a) and (10b) using σ_0 ($b = 0$), which is c_σ with a strength gradient, and as normalized do not depend Φ.

The exact size of the domain of integration in Eq. (3) need not be specified to assess the initiation angle and relative mixed-mode toughness for homogeneous material, as these quantities involving integrations over the classical K-field are independent of the choice of radii. However, determining effects of a strength or modulus gradient on fracture behavior for an FGM requires specification of these dimensions, as it is precisely the gradient-induced variations away from the crack tip that alter the fracture characteristics. Only for sufficiently shallow gradients (low b), or for fracture processes dominated by the very near-tip fields (high m), will the relevant character of the crack fields be the same as in the homogeneous case. Several examples with sigmoidal variations in σ_0 or E are examined with two sets of integration limits in the r-direction, $\rho = R/10^3$ and $R/10^5$, before generalizing results.

5.2.1. Parallel strength gradient, $\sigma_0(x)$

For a graded material with a parallel variation in strength $\sigma_0(x)$ and nominal mode I loading, symmetry dictates a solution with no kinking on average, $\phi = 0$. However, the initiation fracture toughness K_Φ, i.e., the stress-intensity factor that will result in a stated first failure probability (say 50% or 90%), is affected by the gradient strength.

Results for the normalized toughnesses are displayed in Fig. 7, for m from 2 to 11 and $b(2R) = \{-20, 20\}$. For gradients in strength with $b < 0$, which correspond to cases of cracks growing into weaker material, there is, as expected, a reduction in predicted initiation toughness. The effect is very strong for lower m, as the failure behavior is increasingly volume dependent, and farther ahead of the crack tip larger volumes of weak material are sampled. However, for cracks growing into stronger material ($b > 0$), a similar, but smaller, degradation of initiation toughness trend is also evident, except for very small b. This reduction derives from the sampling of all material in the neighborhood of the crack tip, not just that in front, $x > 0$. The material located outside $-\pi/2 < \theta < \pi/2$ is weaker than that just ahead of the crack tip, and the steeper the gradient, the weaker that material. Given that the maximum principal stress at $\theta = \pm 114°$ is the same as it is at 0° (see Fig. 1), this weakness greatly affects the probability integral, although not as much as for a negative gradient.

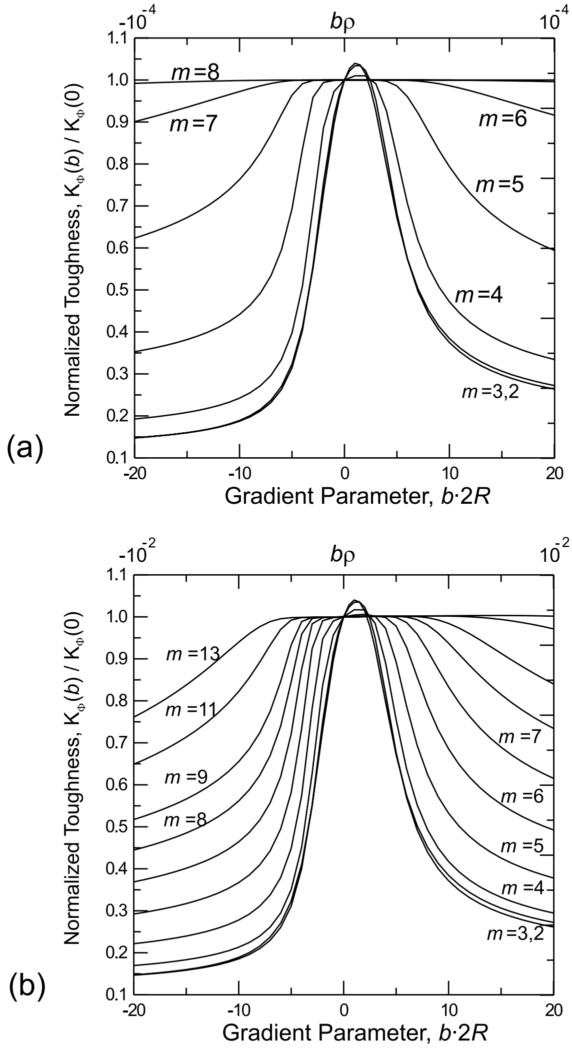

Fig. 7. Mode I fracture toughness for an infinite body FGM with $\sigma_0(x)$ based on statistical model. Results are displayed for two sets of integration limits, ρ and R, with (a) $\rho = R/10^5$ and (b) $\rho = R/10^3$ and m from 2 to 13.

As with homogeneous mixed-mode fracture (Section 5.1), these results must be carefully interpreted. Although material fracture is expected at a lower applied K than in the homogeneous case, a cracking event behind the main crack tip is unlikely to trigger total failure of the body, but rather would lead to a zone of widely distributed damage, or to a discontinuous crack extension that would later produce a bridged crack.

5.2.2. Infinite body with parallel stiffness gradient, $E(x)$

Fig. 8 shows the range of predicted toughness for $E(x)$ gradients. The strength, σ_0, is taken to be constant. Results displayed show a toughening for $b < 0$ and low values of m. That is, for a given crack-tip K, failure is less probable for cracks growing into more compliant material. In contrast, large reductions in toughness are seen for $b > 0$, but again only for relatively low m.

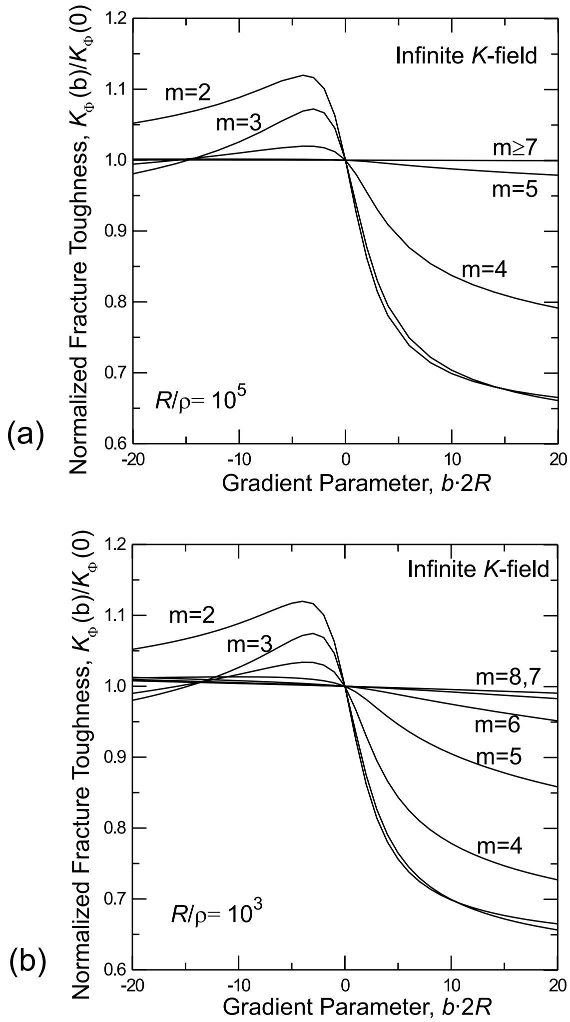

Fig. 8. Mode I fracture toughness for an infinite body FGM with $E(x)$ based on statistical model. Stress field is a one-term modification of the homogeneous field (Eq. (2)). Results are displayed for two sets of integration limits, (a) $\rho = R/10^5$ and (b) $\rho = R/10^3$, and m from 2 to 8.

The effect is clearly a result of the form of the stress field, the FGM modification of the classical field (Eq. (2)). [4] For cases with elevated stresses ahead of the crack, $b > 0$, the failure probability is increased, and thereby the toughness is decreased. The opposite is true of the $b < 0$ case at modest levels of $-b$, where stresses ahead of the crack are lower for a given K.

5.2.3. Infinite body with perpendicular strength gradient, $\sigma_0(y)$

The classical formulae for crack kinking indicate the preferred direction for extension to be along 0° for mode I loading, but for an FGM with a normal gradient in the Weibull strength, $\sigma_0(y)$, the spatial variation

[4] Commentary on the accuracy of this approximation can be found in Section 5.3.3.

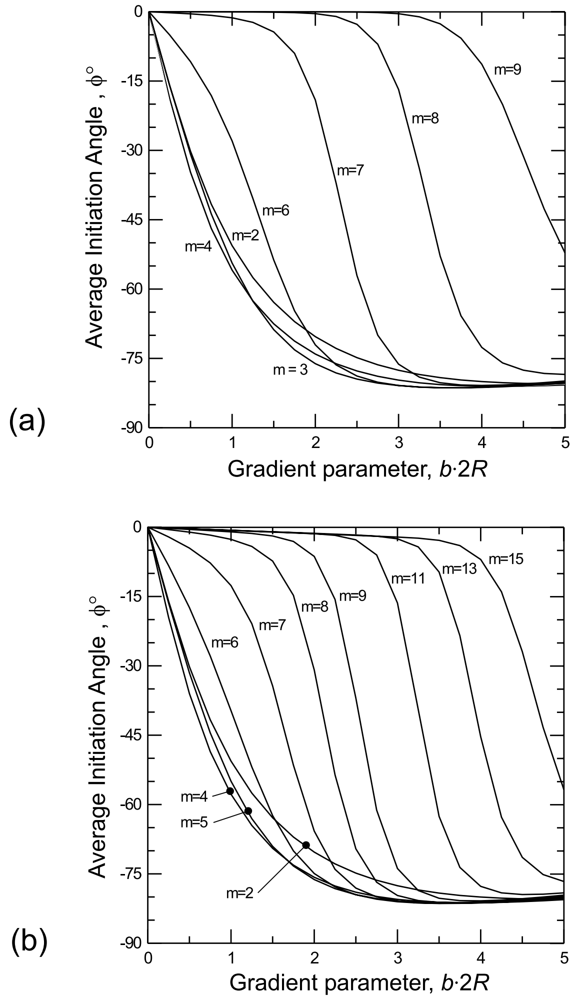

Fig. 9. Average initiation angle ϕ for an infinite body FGM with $\sigma_0(y)$ based on statistical model. Results are displayed for two sets of integration limits, (a) $\rho = R/10^5$ and (b) $\rho = R/10^3$, and m from 2 to 15.

in strength results, on average, in a preferred nonzero initiation angle, ϕ. Fig. 9 shows the range of predicted ϕ, and as results are an odd function of the gradient strength ($\phi(b) = -\phi(-b)$), only for a positive range of $b(2R) = \{0, 5\}$. A strong dependence on $\sigma_0(y)$ is observed, with the average initiation angle approaching 80° for very low Weibull modulus ($m < 5$). Even with higher m, a transition occurs to cracking at 80° although the critical gradient for this transition increases sharply with m.

Note that toughness results for $\sigma_0(y)$ exhibit similar trends as for the case of $\sigma_0(x)$, degradation of toughness. The actual curves are more similar to the $b < 0$ region of Fig. 7. So, not only will the crack tend to grow into the weaker material with a variation in strength present, $\sigma_0(y)$, but fracture will initiate at a lower applied K than in the homogeneous case.

5.2.4. *Infinite body with normal stiffness gradient, $E(y)$*

Crack initiation was studied for infinite bodies with $E(y)$ in two ways, each with σ_0 held constant. First, the effects of gradient-induced terms in the stress field are examined by using a pure mode I field near the tip

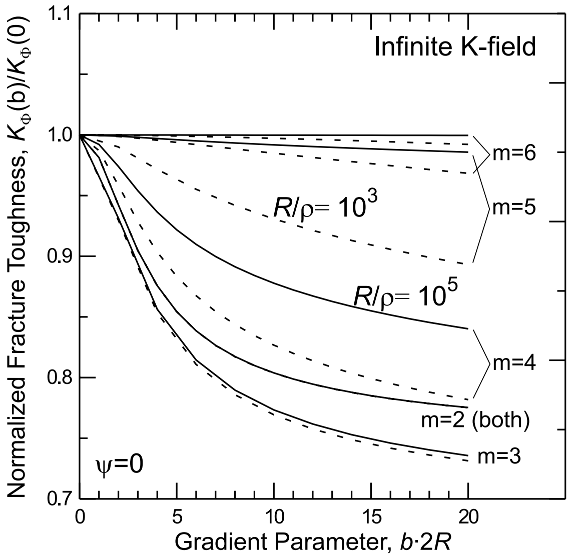

Fig. 10. K_Φ for infinite body with the modified K-field (Eq. (2)) and a gradient in Young's modulus normal to the crack, $E(y)$. The near-tip region is in pure mode I loading, but the modulus gradient induces an asymmetry in stresses. The elevated stresses in a region $y > 0$ for $b > 0$ cause the failure probability to be increased for a given K.

with the $E(y)$ modification via Eq. (2). Fig. 10 displays the gradient effect on toughness for $b(2R) = \{0, 20\}$. A degradation of over 25% compared to the homogeneous case is evident for low m (2,3), purely due to the elevated stress in the regions of material with higher modulus $E(y)$.

In general, the existence of a stiffness gradient normal to the crack plane causes mixed-mode loading at the crack tip [3]. The FGM stress field depends on the geometry-specific relationship between the modulus gradient and phase angle. The average initiation angles for an infinite sample with a range of Weibull moduli, $m = \{2, 11\}$, are displayed in Fig. 11 for a range of $b(2R) = \{0, 20\}$ (as ϕ is an odd function of b). The stress field is again approximated by Eq. (2); however, the phase angles used are increased with b to match the $\psi(b)$ data of the calibration curve of the SE(T) specimen (subsequently in Fig. 13, Section 5.3.1), which will facilitate later comparison.

For high m, results for this FGM field agree reasonably well with the cracking angles for a homogeneous stress field (Fig. 6) at the same ψ. For instance, for $b = 10$, $\psi = 18.1°$, and for $m = 9$–15, $\phi_{\mathrm{FGM}} = -50°$ to $-60°$, which is similar to that for homogeneous materials at this ψ. At low m, the agreement is poor, with cracking angles being much nearer to zero for graded materials. This difference arises because for the high m, small ρ situation, cracking is dominated by the stresses very near the tip, which, being essentially those of the classical Williams K-field, are affected by the gradient primarily through the phase angle, ψ. As the gradient is made steeper (from $b \sim 10$–20), this phase angle nearly plateaus. However, the assumed multiplicative effect of the modulus field on the stress field, Eq. (2), does not change in form as the gradient becomes steeper. Thus, from Eq. (2), for a fixed phase angle, an increase in modulus will raise all the stresses at $y > 0$ (relative to those in the homogeneous case with the same ψ). The resulting sampling of the whole body will recognize this elevated stress level; for sufficiently low m, it will dominate, as implied by the insensitivity to ρ for small m. Thus, the near-tip stresses for $\psi > 0$ drive the crack in the negative y-direction while the far-field stresses drive the crack in the positive y-direction, because the scaling by $E(y)$ dominates the effect of ψ. This also leads to the average initiation angle being notably smaller (less negative) in some FGMs computed with larger ρ, i.e., for intermediate m.

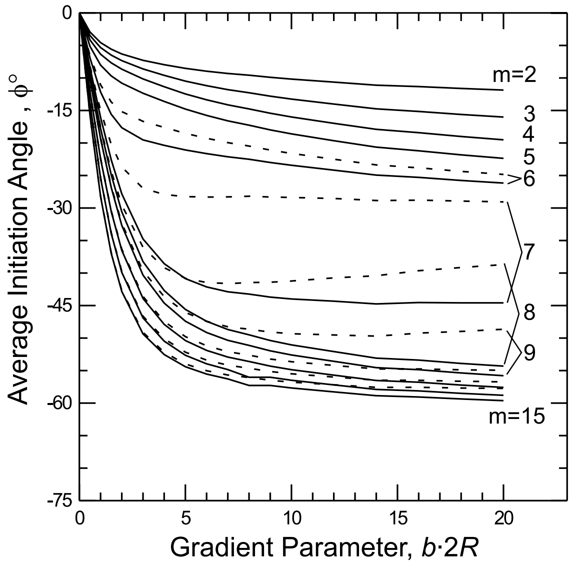

Fig. 11. Average initiation angle ϕ, for an infinite body FGM with $E(y)$ based on statistical fracture model. Stress field is the one-term modification of the homogeneous stress field (Eq. (2)), plus ψ is increased with b (see text). Results are displayed for two sets of integration limits with $\rho = R/10^5$ (solid lines) and $\rho = R/10^3$ (dashed lines) and m from 2 to 15.

5.2.5. Implications

Gradients in material properties affect the toughness in several distinct ways, including the initiation toughness and the crack angle and its dispersion. Both have implications for the final fracture behavior.

The trends depicted previously, as well as the expected behavior for other conditions, can be understood in terms of the most probable radial distance from the crack tip for cracking to initiate. The local cumulative cracking probability is $p(\sigma)\,\mathrm{d}V/V_0$, and so the fracture probability in an annulus at a given radial distance from the tip scales with $\int_{-\pi}^{\pi} p(\sigma)r\,\mathrm{d}\theta$. Thus, important trends are revealed by the behavior of the weighted probability function $p^*(K,r) \equiv p(\sigma(r))r$, based on $p(\sigma)$ as given in Eq. (11), (for which $\sigma(r)$ is from Eq. (2)) and with the gradient aligned along a direction of high stress for the crack, i.e., high $f_1(\theta,\psi)$, and b selected to give relative weakening (high E/σ_0) ahead of the crack.

In a homogeneous material, cracking frequencies decrease with increasing r for all $m > 2$ in a linear-elastic stress field. However, for a sigmoidal gradient in either σ_0 or E, under certain conditions a local minimum and maximum in p^* exist at radial positions r_n and r_x, respectively, as depicted in Fig. 12. These occur such that $0 < r_n < r_x$, and they scale with $1/b$, as described in Appendix B.

A key issue concerns the strength of the maxima, specifically the relative values of σ/σ_0 and especially of p^* at r_x vs. at the cutoff distance ρ. The cases of $\sigma_0(x)$ with $b(2R) = -20$ and of $E(x)$ with $b(2R) = 20$ for $m = 3$ and 11 provide an illustrative range of examples to examine. Values for $r_x b$ (from Eqs. (B.1) and (B.2)) are listed in Table 2 as are ratios of σ/σ_0 and of p^* (at r_x vs. at ρ) (from Eqs. (B.4a) and (B.4b)) taking $b\rho = 10^{-4}$ and 0.01, the limiting conditions for the plots in Figs. 7–11. For most of these cases, maxima exist for the weighted probability p^*, but they span a range from the local peak in σ/σ_0 (being low but relevant) vs. the value at ρ to $\sigma/\sigma_0(r_x)$ (being too small to influence the cracking probability).

By extending the arguments made regarding the crack locations in homogeneous materials (Table 1) in light of information in Table 2 and Figs. 7 and 8, it is argued that for FGMs the predominant region of failure can be categorized into three situations, at least where the relatively weak region is ahead of the crack, as is described next.

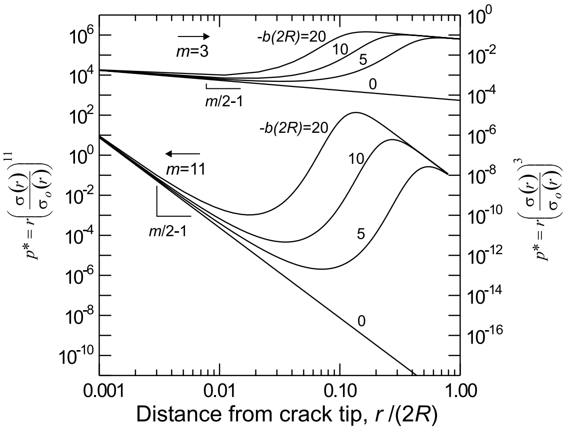

Fig. 12. Variation of the weighted local failure probability $p^*(\sigma)$ for an infinite body with $\sigma_0(x)$ for $m = 3$ and 11. Gradient parameters of $-b(2R) = \{0, 5, 10, 20\}$ are displayed. The tendency for fracture to initiate away from the crack tip is apparent as $p^*(\sigma)$ can reach a local maximum with a value exceeding p^* at ρ.

Table 2
Parameters for local maxima in cracking probability

	$m = 3$		$m = 11$	
For $\sigma_0(x)$, $c = 10$	$\rho b = 0.01$	$\rho b = 0.0001$	$\rho b = 0.01$	$\rho b = 0.0001$
$-r_x b$	3.26	3.26	2.69	2.69
$\sigma/\sigma_0\|_{r_x}/\sigma/\sigma_0\|_\rho$	0.55	0.055	0.61	0.061
$p^*(r_x)/p^*(\rho)$	54.4	5.45	1.12	8.65×10^{-10}
For $E(x)$, $c = \infty$	$\rho b = 0.01$	$\rho b = 0.0001$	$\rho b = 0.01$	$\rho b = 0.0001$
$r_x b$	1.7	1.7	0.6[a]	0.6[a]
$\sigma/\sigma_0\|_{r_x}/\sigma/\sigma_0\|_\rho$	0.14	0.014	0.19	0.019
$p^*(r_x)/p^*(\rho)$	0.475	0.0467	5.56×10^{-7}	5.50×10^{-16}

[a] Inflection only for this condition.

If $m < 4$, the cracking sites are spread widely throughout the crack-tip stress field as for a homogeneous material. As can be appreciated from Fig. 12, if $p^*(r_x)/p^*(\rho) \gg 1$, relatively few failures will occur near the crack-tip region itself. Generally, if $m < 4$ and cracking frequencies exhibit a local maxima, cracking will largely be distributed between r_x and R. Following the logic leading to Eqs. (10a) and (10b), the toughness will vary as

$$K_\Phi \approx \frac{\sigma_0\left(\frac{V_0}{B}\right)^{1/m}\sqrt{2\pi}\left(2-\frac{m}{2}\right)^{1/m}\left(-\ln(1-\Phi)\right)^{1/m}}{\left[\int_{-\pi}^{\pi} f_1(\theta,\psi)^m \,\mathrm{d}\theta\right]^{1/m}} \frac{\sigma_0(\infty)E(0)}{\sigma_0(0)E(\infty)} \Bigg/ R^{(2/m)-(1/2)} \quad (m < 4). \tag{12a}$$

This limiting situation implies that virtually all the cracking occurs at $r > 2/b$, where the tanh functions are saturated. For exact results in the plots of $K_\Phi(b)/K_\Phi(0)$ shown in Fig. 7 for $\sigma_0(x)$ with $b < 0$, and in Fig. 8 for $E(x)$ with $b > 0$, the relative toughnesses for $m = 2$ and 3 are approaching, but have not attained, these limits, $\sim 1/c_\sigma$ and 1/2, respectively, which are insensitive to b and would obtain for $|b(2R)| \gg 20$. Owing to the relative insensitivity to behavior at $r \ll R$, the toughness does not reflect the actual value of $p^*(r_x)/p^*(\rho)$, as is verified by comparing the behavior in Table 2 for $m = 3$, with the exact results in Fig. 7, for $b < 0$ or in

Fig. 8, with $b > 0$, where $K_\Phi(b)/K_\Phi(0)$ for both is insensitive to the value of ρ despite the large differences in $p^*(r_x)/p^*(\rho)$ (Table 2).

For higher m, behavior is determined by whether cracks form just beyond ρ, as in a homogeneous material, with K_Φ nearly unchanged from Eqs. (10a) and (10b) and insensitive to b, or instead are more widely distributed. In behavior more likely to pertain for intermediate m, crack locations would be clustered near r_x if b were large enough that $p^*(r_x) > p^*(\rho)$. From Eqs. (B.4a) and (B.4b), this depends on b and c as well as on the relevant value of ρ needed to describe the fine-scale microstructural variations. For the cases involving $\sigma_0(x)$ illustrated in Fig. 7, where the curves have begun to decline sharply with increasing $-b$, the transition to failure being near r_x has initiated. The transition is largely complete at $-b(2R) = 20$, for $m < 11$ with $b = 0.01$ and for $m < 6$ with $b\rho = 10^{-4}$. This shift cannot occur with a modulus gradient unless $br_0 > 0$. In the limit that most failures occur just at and beyond r_x

$$K_\Phi \propto \sigma_0 \left(\frac{V_0}{B}\right)^{1/m} \frac{\sigma_0(\infty)}{\sigma_0(0)} \frac{E(0)}{E(\infty)} \left(\frac{r_x b}{|b|}\right)^{(1/2)-(2/m)} \qquad (m > 4). \tag{12b}$$

Here, the expected toughness decreases with rising $|b|$ because the stress at the probable cracking location increases with $|b|$ for a given level of K; this follows from Eq. (12b) as $r_x b$ is nearly constant, as shown in Appendix B.

Thus, for FGMs loaded to have a region of high σ/σ_0 ahead of the crack tip, this fracture mechanism involving nonlocal failure is more likely to apply than for homogeneous materials; nonetheless, this applicability still depends, in part, on the value of ρ (or $b\rho$), which reflects other details at the crack tip that preclude direct crack extension being preferable.

The behavior with other gradient alignments or phase angles is more complicated. If a gradient is oriented so that the direction of high E/σ_0 is aligned with the region of high $f_1(\theta, \psi)$ for the stress field, a reduced toughness results with even modest gradient intensities; moreover, the region of damage will be much more focused for both degradation regimes (low and intermediate m) with a gradient present. This is shown in Table 3, which lists the median cracking angles θ_{50} and the dispersion in cracking angles, expressed as $\theta_{75} - \theta_{25}$, for several situations involving gradients in σ_0 with $b(2R) = \{-20, 0, 20\}$ and for $R/\rho = 10^3$. In particular, $\theta_{75} - \theta_{25}$ is smaller if $b < 0$ and $\psi = 0$.

In contrast, if the gradient alignment is opposite, the toughness may rise with modest gradient levels in low-m materials, but diminish for more intense gradients even with higher m values. This is clear in Fig. 7 for variations in $\sigma_0(x)$ and is implied by extrapolating the curves for gradients in $E(x)$ in Fig. 8 to higher levels of $-b$. In essence, material beyond the crack by $r > 1/b(\theta > 0)$ becomes relatively stronger than without a gradient, and so total failure probabilities can be reduced for m low enough that cracking at large r is relevant. However, the degradation in K_Φ with a steeper gradient entails fracture at the crack flanks

Table 3
Effect of gradient on angular dispersion of first fracture locations

$\sigma_0(x)$	$m = 3$		$m = 11$		$\sigma_0(y)$	$m = 3$		$m = 11$	
b	θ_{50}	$\theta_{75} - \theta_{25}$	θ_{50}	$\theta_{75} - \theta_{25}$	b	θ_{50}	$\theta_{75} - \theta_{25}$	θ_{50}	$\theta_{75} - \theta_{25}$
$\psi = 0°$ ($\theta_{\sigma_{\theta\theta}\|max} = 0°$)									
−20	0°	70°	0°	64°	−20°	73°	42°	72°	24°
0	0°	124°	0°	118°	0°	0°	124°	0°	118°
20	0°	244°	0°	124°	20°	−73°	42°	−72°	24°
$\psi = 45°$ ($\theta_{\sigma_{\theta\theta}\|max} = 52°$)									
−20	−19°	51°	−27°	28°	−20°	+46°	39°	−83°	80°
0	−74°	100°	−88°	72°	0°	−74°	100°	−88°	72°
20	−146°	32°	−150°	25°	20°	−90°	57°	−90°	38°

(which is normally unlikely), as shown in Table 3 for $\sigma_0(x)$ at $b > 0$ for which $\theta_{75} - \theta_{25}$ has become very large (244°). From inspection of Fig. 1, it can be seen that if a cracking condition that depended upon the hoop stress, $\sigma_{\theta\theta}$, were pertinent, the tendency of weakening effects to outweigh local strengthening would be lessened owing to the narrower angular range of singular crack-tip stresses.

Based on the tendency for weakening to predominate, it is not surprising that for nonparallel gradient alignments, a decline in initiation toughness generally follows, as for $E(y)$ (Fig. 10), for which the toughness declines with b almost as rapidly as when the gradient is aligned along $E(x)$ with $b > 0$ (Fig. 8).

The probable angle of crack initiation is obviously shifted by the presence of a gradient. It should be noted that the angular location of cracking even when it occurs near ρ can be markedly changed by relatively small levels of b, i.e., at levels having only minimal affects on K_Φ. This emerges from comparing the levels of b that markedly change the crack angle with a gradient in $\sigma_0(y)$ (Fig. 9) with the much larger levels of $-b$ needed to alter the toughness with $\sigma_0(x)$ (Fig. 7). This obtains because the angular dependence of the crack-tip stresses, $f_1(\theta, \psi)$, especially for σ_1, is rather weak over a wide interval, Fig. 1a, and so the angle of the highest stress can be shifted even by a shallow material property gradient.

An equally important issue concerns whether the range in probable crack initiation angles, or the difference in expected initiation angle, ϕ, and stable extension angle, θ^*, is made larger or narrower by the presence of a gradient. Expected trends are again illustrated in Table 3. For situations in which the range of initiation angles is raised with increasing gradient, a microcrack or bifurcation zone would be wide, or more diffuse, especially for low m. This should raise the difference between the loads for first cracking and final failure, i.e., steepen the R-curve. Where the zone of probable cracking is narrower, i.e., focused, the fracture surface will be less rough and the R-curve relatively flatter, e.g., for σ_0 $(b < 0)$.

For mixed-mode loading, the expected microcrack zone tends to be less wide (Table 3). However, the average location depends strongly on m and is unlikely to be on the path of the eventual main crack ($\phi \neq \theta^*$). It is assumed that subsequent cracking would statistically tend to be along the path of maximum $G/G_c(x, y, \theta)$, and the resistance could be heterogeneous as well. When these angles differ, strongly rising R-curve effects could also be very significant.

Thus, the presence of a strength gradient would almost invariably lower the toughness for first cracking; however, unless the weak material were largely ahead of the crack, the corollary effect would be to markedly widen the damage zone perhaps enough to induce a net increase in final toughness if a substantial trend develops toward first cracking occurring near the crack flanks. For modest modulus gradients, the effects on first cracking and final cracking would tend to be the same rather than offsetting unless the gradient were nearly normal to the crack. Thus, situations with some toughening both for first cracking and from a rising R-curve can exist.

Finally, it should be emphasized that if the position of the crack tip is shifted such that $br_0 \sim 1$, the qualitative differences between gradients in σ_0 and E will be switched (as follows from Eqs. (B.1)–(B.3), (B.4a), (B.4b)). That is more toughening would be accessible with σ_0 gradients and more degradation in K_Φ for initiation could derive with modulus gradients, but accompanied by opportunities for R-curve behavior.

5.3. FEA of finite-sized specimens

Although dependencies of the toughness and initiation angle on the modulus gradient emerge for the infinite body FGM (Section 5.2) due to the gradient-induced modification of the K-field, at finite r, other deviations from the classical K-field can also be expected. Even in homogeneous materials for cracks in finite bodies, boundary condition-induced higher-order terms in the Williams expansion will dictate the stress field at increasing distance from the crack tip. Thus, it should be appreciated that with a nonlocal fracture criterion, fracture toughness could depend upon the actual specimen size and geometry, especially for an FGM. By comparing the results for an infinite body (Sections 5.2) and those derived from FEM results for a specific specimen geometry, it can be determined how effects of geometry and gradient are likely to interact or dominate.

After describing the calibration of the single-edge crack tension SE(T) sample, several examples are given in which failure probabilities are computed based on stresses in the entire graded sample excluding a zone within either $\rho = a/10^5$ or $a/10^3$. These toughnesses are normalized to that of a homogeneous body ($b = 0$) for the finite sample, which differs in detail from that in Eqs. (10a) and (10b), and are, thereby, insensitive to the failure probability, Φ, chosen as a basis for comparison. Samples having gradients in either σ_0 or E aligned with the crack tip centered in the gradient ($\varsigma_o, \xi_o = 0$) are assessed.

5.3.1. Specimen calibration

A modulus gradient parallel to the direction of the crack, $E(x)$, retains the symmetry of the homogeneous problem so that $K_{II} = 0$. For homogeneous materials with load boundary conditions, the stress-intensity factor is not influenced by Young's modulus; however, for an FGM, the magnitude of K_I is increased for $b < 0$ and decreased for $b > 0$ as shown in Fig. 13 for the SE(T) geometry with $a = W/2$ (Fig. 3). This behavior is consistent with other observations relating the far-field load and K_I for an FGM with $E(x)$ [3].

Deterministic failure comparisons based on applied loads can be directly inferred from the results of Fig. 13. This indicates that cracks growing into positive b gradients are expected to carry higher loads than homogeneous or negative b materials when fracture is determined by an invariant K_{Ic} or near tip $\sigma_{\theta\theta}$.

The effect of a modulus gradient normal to the crack plane, $E(y)$, is to take a nominally mode I geometry and load the crack tip in both tension and shear. The mixed-mode calibrations for the stress-intensity factors, K_I and K_{II}, are also shown in Fig. 13. K_I is an even function of b, $K_I(b) = K_I(-b)$ and K_{II} is odd. Both stress-intensity factors are amplified with increasing $|b|$, but with a resulting monotonic growth in the tip phase angle, $\psi = \tan^{-1}(K_{II}/K_I)$. This trend seems to plateau for $b(2a) > 10$, as ψ shifts from 0° to 18° while $b(2a)$ goes from 0 to 10 but by only an additional 2° while $b(2a)$ goes from 10 to 20.

The subsequent results depend on the stress field of the entire sample, not just aspects pertinent to the asymptotic crack-tip field, Eq. (1). The deviations of the stresses for a homogeneous material from those of

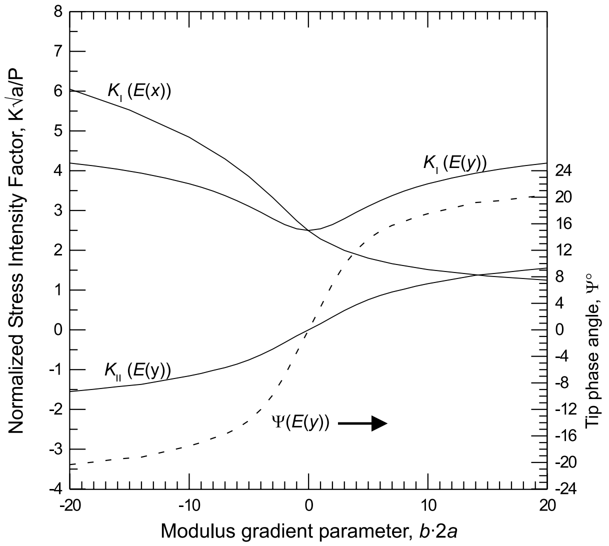

Fig. 13. Stress-intensity factors, K_I and K_{II} for the SE(T) fracture mechanics sample for modulus gradients $E(x)$ and $E(y)$ (solid lines). The gradient in the y-direction results in a shearing of the crack tip, such that that the tensile geometry results in a mixed-mode loading with ψ increasing in magnitude for increasing gradient (dashed line).

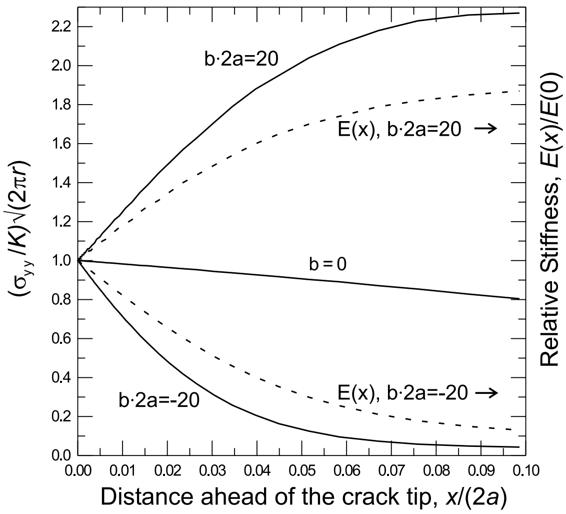

Fig. 14. Deviation of yy-stresses ahead of the crack tip from classical K-field values for an SE(T) specimen with $E(x)$ gradient for cases with $b(2a) = \{-20, 0, 20\}$. Normalized moduli $E(x)$ are plotted for comparison. The approximation in Eq. (2) would appear to better describe the near-tip stresses, but underestimates the magnitude of the gradient-induced adjustment.

the K-field are displayed in Fig. 14 (curve labeled $b = 0$). These stresses deviate weakly from those of the K-field compared to those with an $E(x)$ gradient present, also shown for $b(2a) = \{20, -20\}$.

5.3.2. SE(T) with parallel strength gradient, $\sigma_0(x)$

For an SE(T) sample with strength gradients $\sigma_0(x)$ but homogeneous modulus, E, the variation in the relative fracture toughness, K_Φ, is shown in Fig. 15 as a function of strength gradient with $b(2a) = \{-20, 20\}$. Fig. 15a displays a reduction in toughness for all gradients when $m < 7$. With the larger cutoff region (Fig. 15b), the degradation in toughness occurs for $m \leqslant 11$. The $\rho = a/10^5$ case (Fig. 15a) biases the results toward the homogeneous situation, which lessens the gradient effects on toughness. It is worth noting the general agreement between results in Figs. 7 and 15, the latter of which only utilize the modulus-corrected Williams expansion near the crack tip (but have an outer cutoff R). However, discernable differences exist even for intermediate m values for which most cracking occurs between ρ and r_x.

5.3.3. SE(T) with parallel modulus gradient, $E(x)$

The calculated statistical fracture toughness, K_Φ, for a range of modulus gradients $E(x)$ and uniform strength is plotted in Fig. 16. Clearly, for a crack growing into a stiffer material, the toughness of the structure is decreased for material with low m. Conversely, toughening occurs for cracks growing into a more compliant material.

These results, obtained via FEM analysis of the SE(T) geometry, utilize the complete stress field, and effects are due to both the modulus gradient and the finite geometry. Prior calculations with a linear $E(x)$, rather than a sigmoidal variation, exhibited similar trends, which differed in detail [29]. For either geometry, it can be seen that the loss of toughness with $b > 0$, based on the local K, is offset by the modulus shielding for comparisons based on applied load.

The trends of a large influence of a gradient occurring with low m correspond to the probable location of fracture initiation shifting away from the crack tip, to where the stress solution deviates most from the classical singular form, as depicted in Fig. 14 for the yy-component. These results indicate that although K is a valid scaling parameter for the stress field very near the crack tip for an FGM, the dependence of the

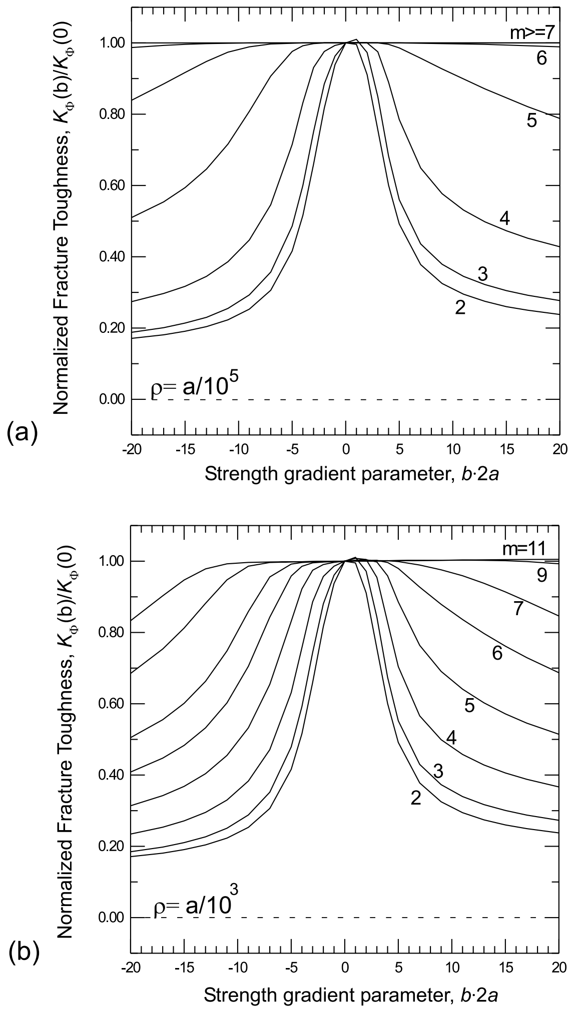

Fig. 15. Effect of variable strength $\sigma_0(x)$ on normalized fracture toughness of an SE(T) specimen. Two near-tip cutoff regions are used, $\rho = a/10^5$ (a) and $a/10^3$ (b).

stresses away from the crack on the gradient in E renders K_Φ to be an inaccurate predictor of failure if it initiates away from the tip. These effects arise because stresses ahead of the tip, and hence the cracking probability, are higher with a positive gradient than would exist for a homogeneous material at the same K.

The trends roughly agree in Figs. 8 and 16; however, the infinite body analysis only utilizes one correction to the singular term in the asymptotic expansion near the crack tip and underestimates the magnitude of gradient effects. The reason can again be seen in Fig. 14. Here the σ_{yy} stress ahead of the crack tip (along $y = 0$) normalized by the K-field value is plotted for $b = \{-20, 0, 20\}$; also plotted are the normalized variations in the elastic modulus for the same gradients. The homogeneous stress solution deviates slowly from the classical K-field, with exact agreement as $x \rightarrow 0$ (by nature of the fitting routine for K) and 10% deviation at $x/a = 0.1$. In contrast, the exact solutions with gradients deviate from the K-field by 10% at $x/a = 0.007$, meaning $x|b| = 0.13$. Eq. (2) describes the stress field in the FGM as that of the homogeneous field multiplied by the pointwise variation in modulus. Fig. 14 demonstrates that although this method-

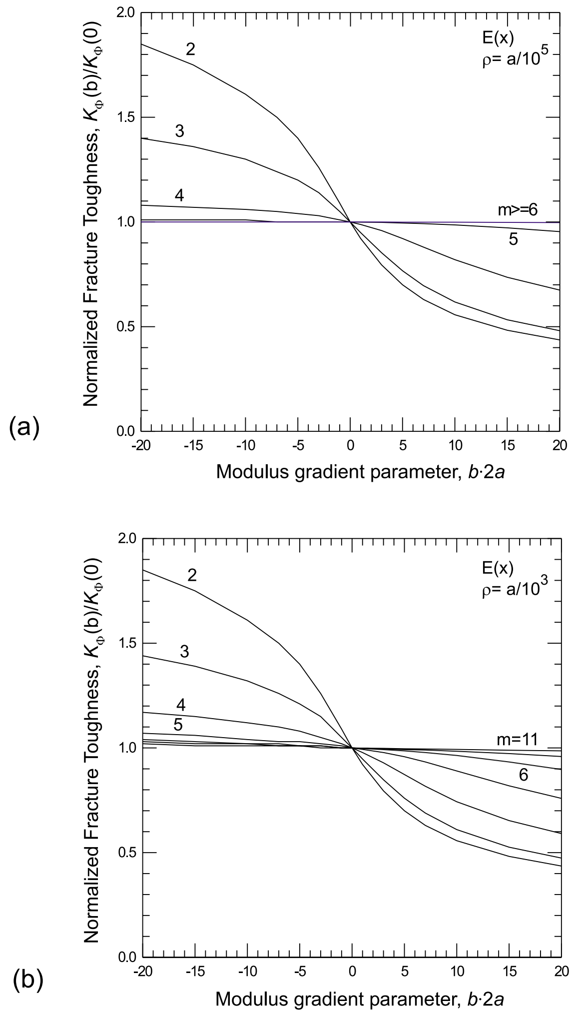

Fig. 16. Effect of variable modulus $E(x)$ on normalized fracture toughness of an SE(T) specimen. Two near-tip cutoff regions are used, $\rho = a/10^5$ (a) and $a/10^3$ (b).

ology yields a better estimate of the stress field than does the Williams K-field, it underestimates the true change for FGMs, even at $x|b| \ll 1$. Evidently, the infinite body analysis of Section 5.2.2 uses a stress field which varies too weakly with b and, especially for $b < 0$, the overall effect on fracture behavior is underestimated. For example, for $m = 3$ and $b = -10$ in the infinite body with the larger cutoff region, $K_\Phi(b)/K_\Phi(0) = 1.03$, and for the SE($T$) geometry, $K_\Phi(b)/K_\Phi(0) = 1.35$.

5.3.4. SE(T) with perpendicular strength gradient, $\sigma_0(y)$

For the SE(T) specimen with normal gradients in strength $\sigma_0(y)$ varying over $b = \{0, 5\}$, the average initiation angle is displayed in Fig. 17. The results agree well with those in Fig. 9, with a large negative initiation angle predicted for a positive gradient, $\phi b < 0$. The lower the value of m, the larger the average initiation angle will be, until $\phi = 90$ at sufficient b. As greater distances from the crack tip participate in the fracture event at low m, the region with lower strength material will predominate. For high m, (>9 for

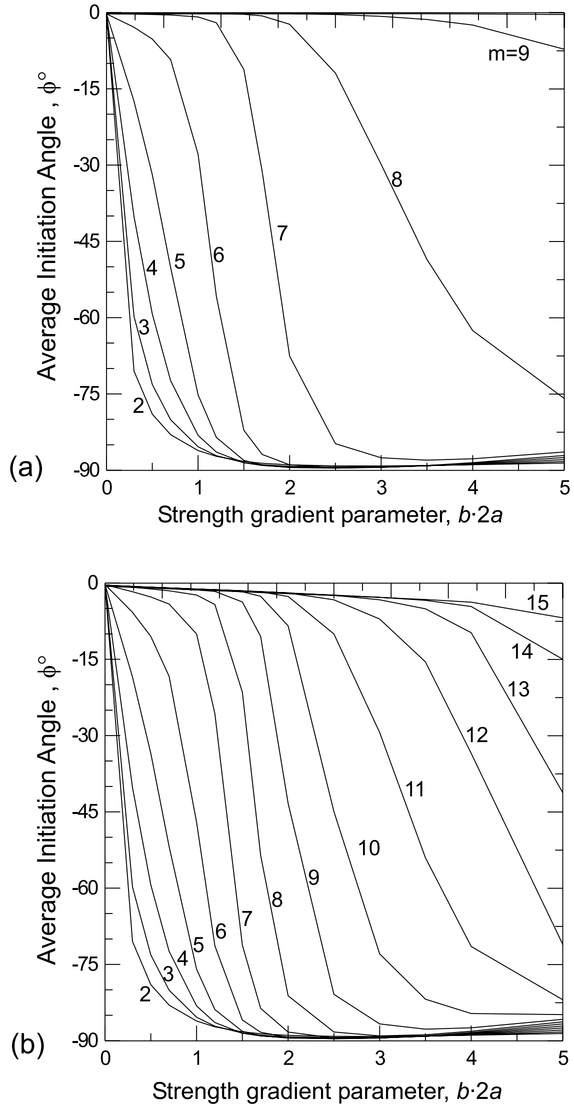

Fig. 17. Average initiation angle for the case of pure mode I loading and $\sigma_0(y)$ in an SE(T) specimen. Strength gradient skews average location of fracture such that nonzero initiation angle is preferred. Two near-tip cutoff regions are used, $\rho = a/10^5$ (a) and $a/10^3$ (b).

$\rho = a/10^5$, >15 for $\rho = a/10^3$), the very near-tip region dominates the calculation for the b levels explored, where the strength variation is limited and the symmetry of the stress field dictates that $\phi = 0$. Overall, the results are similar to those in Fig. 9; however, the sensitivity to increasing m is notably greater for the finite sample, indicating a role for the classical T-stresses (as E is uniform here), which are compressive and not particularly strong for this geometry [45].

5.3.5. SE(T) with perpendicular modulus gradient, $E(y)$

The average crack initiation angles for the SE(T) specimen with a modulus gradient $E(y)$ for a range of m from 2 to 15 are shown in Fig. 18(a). As ϕ is an odd function of gradient strength, only a range of

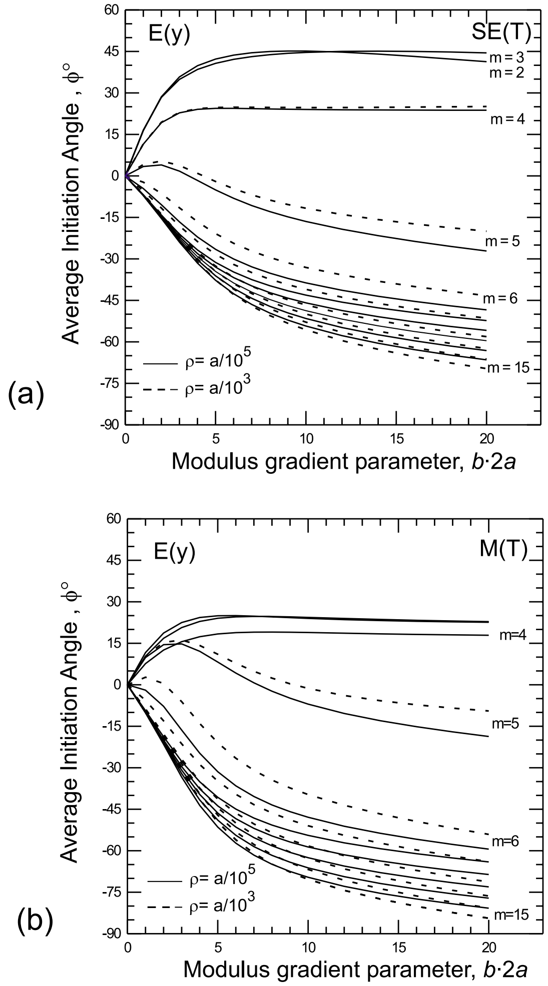

Fig. 18. Average initiation angle with a modulus gradient $E(y)$ in (a) single-edge notched tension, SE(T), and (b) middle-cracked tension, M(T), geometries. The gradient induces a positive crack-tip phase angle as seen in Fig. 13, but the gradient-induced higher-order stresses cause a positive initiation angle for very low m in both geometries.

$b = \{0, 20\}$ is plotted. The dramatic effect of m is evident. First, for high $m(>10)$, positive gradients yield negative initiation angles, i.e., $\phi b < 0$. The high-stress near-tip region of the sample, which experiences a shift in phase angle, dominates these results. As seen for the infinite body analysis for both homogeneous material and FGMs, positive phase angles lead to crack initiation angling downward, $\phi < 0$ for $\psi > 0$.

In contrast, for very low values of $m(\leqslant 4)$, the average direction of initiation is actually positive for positive gradients, $\phi b > 0$. This is, in part, in response to higher stresses associated with the increasing elastic modulus in the positive y-direction, which are only important when cracking is widely distributed. In comparison with the results in Fig. 11, this effect of a gradient with low m is more drastic. This is again due to the fact that Eq. (2) underestimates the effect of $E(y)$ on stresses at finite distances from the crack tip, including treating all components in proportion.

5.3.6. $M(T)$ specimen with perpendicular modulus gradient, $E(y)$

To further elucidate the effect of geometry in the presence of a modulus gradient, a middle-cracked tension ($\mathrm{M}(T)$) fracture mechanics specimen was also analyzed with a variation $E(y)$. When homogeneous, this geometry is known to develop a markedly different stress distribution outside of the K-dominant region. The nonsingular compressive T-stress in the $\mathrm{M}(T)$ sample is nearly five times that in the $\mathrm{SE}(T)$ sample [45]. Also, there is a change in sign in the deviation of the σ_{yy} stress from the K-field due to higher-order geometry terms [46].

The two salient trends, namely tip-dominated, negative angles for $m > 7$, and positive average initiation angles for $m = 2$–4 are evident for both sample geometries. However, the initiation angles for large b are shifted to about 20° lower values for all m for the $\mathrm{M}(T)$ sample. The other differences are mainly expressed for the intermediate m where neither tip nor very far-field stresses dominate. It is interesting to note that the phase angle–gradient relationship for these two samples was found to be very similar, thus indicating that the differences in Fig. 18 arise on the basis of b through higher-order stress terms and not simply through $\psi(b)$ at the tip. At low m, the crack initiation trends in Fig. 18(a) and (b) for the two samples are more similar, compared to the infinite case, Fig. 11, but differences are notable.

Note that recent FEM calculations for a small crack show that the shift in phase angle induced by a normal modulus gradient only develops at a dimension of $rb \sim 1$ [18]. If the effect is similar for these large cracks, then for $m < 4$ material, where most cracking initiates at $rb > 1$, the relevant phase angle would be small and the effect of higher stresses in the stiffer material, at $y > 0$, would appear to dictate the crack locations giving $\phi > 0$.

5.3.7. Implications for fracture experiments and application to FGMs

Effects with far-field mode I loading of FGMs with variable $\sigma_0(x)$, $\sigma_0(y)$, $E(x)$ and $E(y)$ and the crack tip centered in the gradient have been explored. For more general cases with far-field mixed-mode loading and an FGM with arbitrary $\sigma_0(x, y)$ and $E(x, y)$, the space of possible combinations is prohibitively large to survey completely. The results thus far presented for $m > 6$ indicated that behavior is somewhat similar between the finite and infinite bodies. For both situations, the gradient is more influential with larger ρ, and the general similarities indicate that the trends regarding crack location discussed in Section 5.2.5 pertain for finite geometries. Therefore, Eq. (2) for analysis of infinite bodies can be used as in Eq. (11) to anticipate some results of cases not explored here; however, the geometry-induced shifts in phase angle with elastic modulus gradient must be known. Using Eq. (11), it can be observed that as a plausible approximation for real materials, $\sigma_0 \propto E$, and so some of the gradient effects could tend to compensate; nonetheless, large effects of induced ψ, Figs. 5 and 6, still pertain, which may ultimately prove to be more influential at higher m (Figs. 11 and 18).

For lower and intermediate m, the fracture behavior may not be adequately determined by the stresses even within the gradient-corrected K-field of a finite geometry. Even when failure occurs near the crack tip, gradient-induced perturbations influence crack angles (see discussion concerning, Figs. 9 and 11, Section 5.2.5). For these cases, the combined effects of near crack tip, gradient induced and geometry determined stresses must be taken into account. This requires numerical determination of the stress field, e.g., through FEM analyses, which is a more expensive procedure than the semi-analytic modeling of infinite bodies. It is reiterated that when such effects yield first fracture locations that are well away from the eventual crack path for complete failure, various mechanisms may be triggered that can raise the ultimate toughness.

Note that for ductile materials, the nonlinear fracture mechanics is most simply characterized using a single parameter, J; however, this still leads to an appreciable geometry-to-geometry variability in measured crack-growth resistance for many materials. In those materials, the T-stress (or, nearly equivalently, the constraint factor, Q) has been evoked to account for the effects of the next term in the nonlinear stress field expansion about the crack tip [19,47]. This two-parameter characterization allows the description of the material not only at the crack tip, but also at finite distances, and thereby is more successful in determining critical conditions for crack initiation and growth.

The characterization of the stress field in an FGM by the single parameter K has similar limitations. The approximate formulation (Eq. (2)) alludes to the form of the next higher-order term in the expansion. Although in the asymptotic near-tip limit one could also assume the existence of a parallel T-stress, this suffers from the same incompatibility discussed in Section 2. The next-order stress term will therefore not be strictly constant, but using near-tip stresses in an FGM to calculate an effective T-stress may prove to allow for comparison with known effects in homogeneous materials. In a recent study by the authors [18], a kink-length effect was found for the preferred (deterministic) kink angle in an FGM. For kink lengths shorter than the gradient dimension, $1/b$, this effect can almost entirely be accounted for in terms of this effective T-stress, which may depend more on modulus gradient than finite geometry.

It seems clear that the addition of a gradient-induced T-stress can be used to more accurately describe the stress field in an FGM and also provide a more powerful two-parameter scheme to predict statistical crack behavior in different geometries and gradients, at least for the intermediate and high-m material. For longer kink lengths in the above mentioned study, other factors came strongly into play, in part owing to the reduction in induced phase angle for $rb > 1$ already mentioned. Thus, for materials with $m < 4$, in which cracking occurs over dimensions far exceeding $1/b$, further corrections will also be needed. (Actually, ignoring the modulus induced phase shift in conjunction with using Eq. (2) may be a useful approximation at lower m.)

Finally, there are situations in which the stress fields decay rapidly as occurs under an indenter. Then, effects of nonlocal cracking on fracture criteria and causing distributed damage could be great, but using a description based on an asymptotic stress field will be of limited utility.

6. Summary and conclusions

The application of two-parameter Weibull statistics to near-crack fracture problems has been elaborated and extended to the case of mixed-mode loading, with predictions made for both the toughness and average initiation angle of a crack in a brittle material. Conditions have been explored to justify the use of a nonlocal fracture model for brittle materials. This fracture model allows for the statistical correlation between near-tip stresses and first fracture for heterogeneous materials, and possibly for predicting the emergent shape of microcrack damage zones. This is especially interesting for problems in composite-type graded materials (FGMs), where stress fields vary from the homogeneous form away from the crack tip and the strengths can be highly variable throughout. A combination of infinite-body and finite geometry analyses reveal that

- For statistically homogeneous materials, the mixed-mode loading of an elastic crack subject to a nonlocal stress-controlled failure criteria yields a reduction of the fracture toughness by up to 30%, depending on the phase angle ψ and Weibull modulus m. This is roughly 150% of the effect predicted by mechanisms dictated by $\sigma_{\theta\theta}$, usually invoked for continuous kinking.
- The location of microcracks initiated by the main crack stress field do not coincide with the trajectory determined by maximum energy criteria, usually being at larger angles. Thus, diffuse damage zones and crack bridging may develop, thereby, expectedly leading to R-curve toughening for materials that fail by crack initiation away from the main crack.
- Gradients in Weibull scaling stress σ_0 lead to a dramatic decrease in initiation toughness for most alignments of the gradient. However, for cracks growing into stronger, $b > 0$, materials or with gradients normal to the crack $\sigma_0(y)$, weakening for first fracture will involve crack growth initiating at angles that may induce R-curve toughening that will offset this drop in toughness for final failure.

- Calibration of effects of gradients in modulus $E(x)$ for a single-edge notched fracture mechanics specimen show an increased stress-intensity factor for cracks growing into more compliant materials, and crack-tip shielding when growing into a stiffer material.
- When comparing FGMs with gradients in Young's modulus, E, and the same crack-tip stress intensity, the crack growing into the steeper negative gradient, $b < 0$, will be tougher for moderate gradients; whereas most other alignments and very steep gradients lead to a loss of initial toughness.
- Gradients in modulus $E(y)$ for a $\mathrm{SE}(T)$ or $\mathrm{M}(T)$ fracture mechanics sample lead to initiation behavior qualitatively similar to that in homogeneous materials having the same phase angle for $m > 5$, with the average angle $\phi < 0$ for $b > 0$; for lower Weibull modulus though, further effects of an elastic modulus gradient on the stress field cause the average fracture initiation site to be skewed toward the stiffer (higher stress) region, $\phi > 0$ for $b > 0$.
- Infinite-body analyses predict many of the gradient-induced features seen in a finite geometry. When comparing two fracture-mechanics specimen geometries, additional gradient effects on crack-initiation angle were found to be important. There is scope for further analysis that explores the several higher-order terms indicated to be important in the stress fields for FGMs.
- The evolution of damage near a crack tip will vary strongly with the Weibull modulus, m, of the material. For low m materials, a distribution of damage is expected before catastrophic crack advance. The effects of considering ''action-at-a-distance'' are many-fold. Most importantly, the first flaws to be activated in a mixed-mode loading are most likely not in line with what is considered to be the energetically most favorable path. Therefore, it is expected that materials with wide distributions of strength will develop diffuse damage zones around the crack tip. At elevated loads, one expects that these microcracks will link up, or the main crack will jump beyond this damage zone. Under either scenario, the tearing or bridging that results will act as an R-curve mechanism. These effects could be greater in FGMs than for nominally homogeneous materials.

Acknowledgements

This work was supported by Director, Office of Science, Office of Basic Energy Sciences, Materials Sciences Division of the US Department of Energy under Contract no. DE-AC03-76SF00098. The authors would like to thank Prof. Panos Papadopoulos for supplying the finite element code FEAP, and Dr. James M. McNaney and Prof. Daryl Chrzan for helpful discussions regarding Section 3.

Appendix A. Monte Carlo simulations

To illustrate the effects of the elastic near-tip stress field on a material with strength described by Weibull statistics, a Monte Carlo simulation was performed. A domain, 200 units square, was considered with a crack tip at the center {0,0}. For the reasons discussed in Section 3.2, a region (with radius 1 unit) was excluded surrounding the crack tip. For each loop in the simulation algorithm:

- Select random location within the domain (outside of the region of exclusion).
- For element with size $\Delta V = r\,\delta r\,\delta\theta$,centered at $\{x,y\}$, compute $\Phi^{\Delta V}$ from Eq. (3) and Williams stress field (Eq. (1)), $\delta r = 0.1$ unit and $\delta\theta = 10°$.
- Select random $\{\Phi^{\Delta x}_{\text{test}}\}$ (between 0 and 1)

$$\Phi^{\Delta x}_{\text{test}} < \Phi^{\Delta x} \to \text{“hit”; the value of } \{x,y\} \text{ is stored as } \{x,y\}^{\text{hit}}_i;\ N^{\text{hits}} = N^{\text{hits}} + 1$$

$$\Phi^{\Delta x}_{\text{test}} > \Phi^{\Delta x} \to \text{“miss”; the value of } \{x,y\} \text{ is discarded}$$

Fig. 1 displays the results of 5×10^6 runs. From these results, averages can be calculated from the location of the "hits".

$$x^{\mathrm{ave}} = \frac{1}{N^{\mathrm{hits}}} \sum_{i=1}^{N^{\mathrm{hits}}} x_i^{\mathrm{hit}} \qquad y^{\mathrm{ave}} = \frac{1}{N^{\mathrm{hits}}} \sum_{i=1}^{N^{\mathrm{hits}}} y_i^{\mathrm{hit}}.$$

For this average location, the angle is $\tan^{-1}(y^{\mathrm{ave}}/x^{\mathrm{ave}})$. For the mode I case, this is 4.3°. For a phase angle of $\psi = 45°$ case, the angle of the average location is 80.7°. The different mode loading also resulted in a greater number of "hits" (fracture initiations), with 111 hits for the mode-case and 764 for the mixed-mode case.

Appendix B. Derivation of the weighted probability function maxima and minima

As discussed in Section 5.2.5, the incremental fracture probability in an annulus at a given radial distance from the tip depends on $\int_{-\pi}^{\pi} p(\sigma) r \,\mathrm{d}\theta$. As such, important trends are revealed by the behavior of the weighted probability function $p^*(K, r) \equiv p(\sigma r) r$, where $p(\sigma)$ is given in Eq. (11).

When the gradient is aligned along a direction of high $f_1(\theta, \psi)$ with b selected to give relative weakening ahead of the crack, local minima, at r_n, and maxima, at r_x, in failure probability can occur. The locations can be found based on $\mathrm{d}p^*/\mathrm{d}r = 0$, and it can be ascertained by inspection that these occur such that $0 < r_n < r_x$.

With only a gradient in σ_0 present, along the ray of greatest weakening ($\theta = -\theta_\sigma$ and $\varsigma \to -r$), the local minimum and maximum in $p^*(K, r)$ are at positions that satisfy

$$br = \left(\frac{m-2}{8m}\right)\left(\frac{c_\sigma}{c_\sigma - 1}\right)\left[\frac{\mathrm{e}^{2b(r-r_0)}}{c_\sigma} + 2 + \frac{(2c_\sigma - 1)}{c_\sigma}\,\mathrm{e}^{-2b(r-r_0)}\right]. \tag{B.1}$$

By inspection, it can be shown that for $c_\sigma > 2.3$, such a maximum exists for nearly all $m > 2$; if $r_0 = 0$, the maximum typically occurs where $r_x b \approx 2$–3, being larger at lower m. Instead, with a gradient in E, along a ray aligned toward the stiffer direction ($\theta = \theta_E$ and $\xi \to r$), which corresponds to that of rising stress, then r_n and r_x, satisfy

$$br = \left(\frac{m-2}{8m}\right)\left(\frac{c_E}{c_E - 1}\right)\left[\frac{\mathrm{e}^{2b(r-r_0)}}{c_E} + 2 + \frac{(2c_E - 1)}{c_E}\,\mathrm{e}^{-2b(r-r_0)}\right]. \tag{B.2}$$

The existence condition for a maximum, derived assuming $b(r - r_0) \equiv b\Delta r \gg 0$ (so that $\exp -b\Delta r \sim 0$), can be expressed as

$$br > \left(\frac{m-2}{4m}\right)\left(\frac{c_E}{c_E - 1}\right) + \frac{1}{2} - \frac{1}{2}\ln\left[\left(\frac{4m}{m-2}\right)\left(\frac{c_E - 1}{2c_E - 1}\right)\right]. \tag{B.3}$$

For large c_E and $r_0 = 0$, a maximum exists only if $m < 4.51$; usually $r_x b \approx 1$–2, being larger at smaller m.

For either type gradient, if $m = 2$, then $r_n \to 0$ and $r_x \to \infty$. The rise in $\sigma(r)$ owing to the change in $E(\infty)/E(0)$ is only $(2c_E - 1)/c_E$ if $r_0 = 0$; so an actual maximum is less likely to occur than with a gradient in σ_0 where the corresponding ratio is $1/c_\sigma$. However, with a crack tip displaced back from the gradient center, $br_0 > 0$, the modulus change ahead of the crack tip is greater and the behavior would be more like that with a gradient in σ_0 and $r_0 = 0$, as can be seen better in the following.

One important issue concerns the strength of the maxima, in particular the relative values of σ/σ_0 and especially of p^* at r_x vs. at the cutoff distance ρ. The latter is described by

$$\frac{p^*(r_x)}{p^*(\rho)} = \left(\frac{\rho b}{r_x b}\right)^{(m/2)-1}\left(\frac{c_\sigma}{-(c_\sigma - 1)\tanh(r_x b) + c_\sigma}\right) \approx \left(\frac{\rho b}{r_x b}\right)^{(m/2)-1} c_\sigma^m, \tag{B.4a}$$

$$\frac{p^*(r_x)}{p^*(\rho)} = \left(\frac{\rho b}{r_x b}\right)^{(m/2)-1}\left(\frac{-(c_E-1)\tanh(r_x b)+c_E}{c_E}\right) \approx 2^m\left(\frac{\rho b}{r_x b}\right)^{(m/2)-1}, \tag{B.4b}$$

respectively, for a gradient in σ_0 and for a gradient in E with c_E being large.

From Fig. 1a, it can be seen that the major contributions to the angular integrations occur over an interval often exceeding $-2\pi/3 < \theta < 2\pi/3$ for the principal stress, but this does depend on the gradient strength. Thus, log–log plots of $\int_{-\pi}^{\pi} p(\sigma) r\,\mathrm{d}\theta$ vs. r would be similar to that of p^* vs. r in Fig. 12, but adjusted owing to the r- and b-dependence of the angular integration. Specifically, with the gradient aligned parallel to the crack so as to give relative weakening, these adjustments would reduce the effects of stress variations at very high angles from the crack plane and so flatten the local maximum somewhat. They would also slightly increase the distance needed to reach the second asymptotic portion of the curve and would reduce the level of that portion of the curve for low m by a factor near unity from that expected based on the ratio of $\sigma/\sigma_0|_\infty/\sigma/\sigma_0|_0$ along the gradient. Owing to this rather weak sensitivity of the angular term, the results from Eqs. (10a) and (10b) can be applied to give estimates of the limiting toughness for large b for two situations; these are given in Eqs. (12a) and (12b) based upon values from Eqs. (B.1) and (B.2).

It is unclear, however, how these relations pertain in the limit as $b \to \infty$ where other pathologies described for interface cracks would develop, such as singularities in K (e.g., Refs. [16,48]). However, the form of the phase shifts for cracking parallel to an interface are quite different than that for the graded material and a T-stress develops at dimensions small compared to the gradient change that has no counterpart in the solutions for sharp interface cracks which pertain only for $rb \gg 1$ [18].

References

[1] Parsons WB. Engineers and engineering in the renaissance. Baltimore, MD: Williams and Wilkers; 1939.

[2] Weibull W. A statistical distribution function of wide applicability. J Appl Mech 1951;18:293.

[3] Erdogan F. Fracture mechanics of functionally graded materials. Compos Engng 1995;5:753–70.

[4] Ishibashi H, Tobimatsu H, Matsumoto T, Hayashi K, Tomsia AP, Saiz E. Characterization of Mo–SiO_2 functionally graded materials. Metall Mater Trans A 2000;31A:299–308.

[5] Lee CS, DeJonghe LC, Thomas G. Mechanical properties of polytypoidally joined Si_3N_4/Al_2O_3. Acta Mater 2001;49:3767–73.

[6] Sand Ch, Adler J, Lenk R. A new concept for manufacturing sintered materials with a three-dimensional composition gradient using a silicon carbide–titanium carbide composite. Mater Sci Forum 1999;308–311:65–70.

[7] Krell T, Schulz U, Peters M, Kayseer WA. Graded EB-PVD alumina–zirconia thermal barrier coatings—an experimental approach. Mater Sci Forum 1999;308-311:396–401.

[8] Erdogan F. The crack problem for bonded nonhomogeneous materials under antiplane shear loading. J Appl Mech 1985;52:823–8.

[9] Jin Z, Noda N. Crack-tip singular fields in nonhomogeneous materials. J Appl Mech 1994;61:738–40.

[10] Williams ML. On the stress distribution at the base of a stationary crack. J Appl Mech 1957;79:109–14.

[11] Konda N, Erdogan F. The mixed mode crack problem in a nonhomogeneous elastic medium. Engng Fract Mech 1994;47:533–45.

[12] Jin Z-H, Batra RC. Some basic fracture mechanics concepts in functionally graded materials. J Mech Phys Solids 1996;44:1221–35.

[13] Becker TL, Cannon RM, Ritchie RO. An approximate method for residual stress calculation in functionally graded materials. Mech Mater 2000;32:85–97.

[14] Erdogan F, Sih GC. On the crack extension in plates under plane loading and transverse shear. J Basic Engng 1963;85:519–27.

[15] Cotterell B, Rice JR. Slightly curved or kinked cracks. Int J Fract 1980;16:155–69.

[16] Hutchinson JW, Suo Z. Mixed mode cracking in layered materials. Adv Appl Mech 1992;29:64–191.

[17] Gu P, Asaro RJ. Crack deflection in functionally graded materials. Int J Solids Struct 1997;34:3085–98.

[18] Becker TL, Cannon RM, Ritchie RO. Finite crack kinking and T-stresses in functionally graded materials. Int J Solids Struct 2001;38:5545–63.

[19] Larsson SG, Carlsson AJ. Influence of non-singular stress terms and specimen geometry on small-scale yielding at crack tips in elastic–plastic materials. J Mech Phys Solids 1973;21:263–77.

[20] Ishibashi H, Saiz E, Tomsia AP. Powder processing of Mo/SiO_2 FGMs fabricated by slip casting. Am Ceram Soc Bull 1997;76:231.

[21] Ritchie RO, Rice JR, Knott JF. On the relationship between critical stress and fracture toughness in mild steel. J Mech Phys Solids 1973;21:395–410.
[22] Lin T, Evans AG, Ritchie RO. A statistical model of brittle fracture by transgranular cleavage. J Mech Phys Solids 1986;34:477–97.
[23] Lei Y, O'Down NP, Busso EP, Webster GA. Weibull stress solutions for 2D cracks in elastic and elastic–plastic materials. Int J Fract 1998;89:245–68.
[24] Lin T, Evans AG, Ritchie RO. Statistical analysis of cleavage fracture ahead of sharp cracks and rounded notches. Acta Metall 1986;34:2205–16.
[25] Hutchinson JW. Singular behavior at the end of a tensile crack in a hardening material. J Mech Phys Solids 1968;16:13–31.
[26] Rice JR, Rosengren GF. Plane strain deformation near a crack tip in a power law hardening material. J Mech Phys Solids 1968;16:1–12.
[27] Beremin FM. A local criterion for cleavage fracture of a nuclear pressure vessel steel. Metall Trans A 1983;14A:2277–87.
[28] Evans AG. Statistical aspects of cleavage fracture in steel. Metall Trans A 1983;14A:1349–455.
[29] Becker TL, Cannon RM, Ritchie RO. A statistical RKR fracture model for the brittle fracture of functionally graded materials. Mater Sci Forum 1999;308–311:957–62.
[30] Zienkiewicz OC, Taylor RL. The finite element method. New York, NY: McGraw-Hill; 1987.
[31] Stern M, Becker EB. A conforming crack tip element with quadratic variation in the singular fields. Int J Numer Meth Engng 1978;12:279–88.
[32] He M-H, Hutchinson JW. Kinking of a crack out of an interface. J Appl Mech 1989;56:270–8.
[33] Rühle M, Claussen N, Heuer AH. Transformation and microcrack toughening as complementary processes in ZrO_2-toughened Al_2O_3. J Am Ceram Soc 1986;69:195–9.
[34] Rühle M, Evans AG, McMeeking RM, Charalambides PG, Hutchinson JW. Microcrack toughening in zirconia toughened alumina. Acta Metall 1987;35:2701–10.
[35] Wu CCm, Freiman SW, Rice RW, Mecholsky JJ. Microstructural aspects of crack propagation in ceramics. J Mater Sci 1978;13:2659–70.
[36] McClintock FA. A three-dimensional model for polycrystalline cleavage and problems in cleavage after extended plastic flow or cracking. In: Chan KS, editor. Cleavage fracture. George R Irwin Symp. Warrendale, PA: TMS; 1997. p. 81–94.
[37] Mai Y-W, Lawn BR. Crack stability and toughness characteristics in brittle materials. Ann Rev Mater Sci 1986;16:415–39.
[38] Hutchinson JW. Crack tip shielding by micro-cracking in brittle solids. Acta Metall 1987;35:1605–19.
[39] Evans AG. High toughness ceramics. Mater Sci Engng 1989;A105–106:65–75.
[40] Becher PF. Microstructural design of toughened ceramics. J Am Ceram Soc 1991;74:255–69.
[41] Rödel J. Interaction between crack deflection and crack bridging. J Eur Ceram Soc 1992;10:143–50.
[42] McClintock FA, Zaveral F. An analysis of the mechanics and statistics of brittle crack initiation. Int J Fract 1978;25:107–18.
[43] Rice JR, Johnson MA. The role of large crack tip geometry changes in plane strain fracture. In: Kanninen M, Adler W, Rosenfield AR, Jaffee R, editors. Inelastic behavior of solids. NY: McGraw-Hill; 1970. p. 641–72.
[44] Hong T, Smith JR, Srolovitz DJ. Theory of metal-ceramic adhesion. Acta Metall Mater 1995;43:2721–30.
[45] Sherry AH, France CC, Goldthorpe MR. Compendium of *T*-stress solutions for two- and three-dimensional cracked geometries. Fatigue Fract Engng Mater Struct 1995;18:141–55.
[46] Knott JF. Fundamentals of fracture mechanics. London: Butterworth; 1973.
[47] Du ZZ, Hancock JW. The effect of non-singular stresses on crack-tip constraint. J Mech Phys Solids 1991;39:555–67.
[48] Bleeck O, Munz D, Schaller W, Yang YY. Effect of a graded interlayer on the stress intensity factor of cracks in a joint under thermal loading. Engng Fract Mech 1998;60:615–23.